Failure modes and energy absorption in Glass Reinforced aluminum (GLARE) hybrid laminates subjected to three-point bending

Anand, Shreyas; Dighe, Nachiket; Gupta, Pranshul; Alderliesten, René; Castro, Saullo G.P.

Important note
To cite this publication, please use the final published version (if applicable).
Please check the document version above.

Failure modes and energy absorption in Glass Reinforced aluminum (GLARE) hybrid laminates subjected to three-point bending

Shreyas Anand [ID], Nachiket Dighe [ID], Pranshul Gupta [ID], René Alderliesten [ID], Saullo G.P. Castro [ID] *

TU Delft Faculty of Aerospace Engineering, Kluyverweg 1, Delft, 2629 HS, Zuid Holland, Netherlands

ARTICLE INFO

ABSTRACT

This paper investigates 3-point bending failure of five different types of GLARE laminates (2A, 2B, 3, 4A and 4B). 73 configurations (419 specimens), with different stacking sequences and aluminum layer thicknesses are tested. Failure mechanisms, effect of stacking sequence, effect of aluminum rolling direction, effect of displacement rate and energy absorption are analyzed. Configurations with predominantly 0° glass fiber layers fail with delamination as the major failure mode, while configurations with predominantly 90° glass fiber layers fail with central cracking as the major failure mode. GLARE 3, with 1:1 ratio of 0° and 90° fibers, fail with an equal mix of delamination and central cracking. A semi-analytical framework that can be used to predict the force versus displacement curve for central cracking failure is proposed and validated.

1. Introduction

GLARE (GLAss REinforced aluminum laminate) laminates are composed of alternating layers of aluminum and glass fiber, offering several superior properties over traditional aluminum alloys which include excellent fatigue characteristics, high strength-to-weight ratio, high corrosion resistance and a high tolerance to impact damage. These attributes have led to the usage of GLARE laminates in a variety of aerospace applications: upper fuselage skin and empennage leading edge in Airbus A380 [1], cargo liner for regional jet aircraft [1], straps for Airbus A400M fuselage frames [2] and forward bulkhead for the Learjet 45 business jet [3].

Certification for crashworthiness is a prerequisite before any aircraft can enter service, this means that an aircraft should be able to absorb impact energy while keeping the deceleration within acceptable limits. However, unconventional designs (such as the flying-V) which combine the lifting (wings) and load bearing (fuselage) structures of the aircraft to achieve higher fuel efficiency pose a difficult challenge for crashworthiness. Since, the fuselage of such aircraft shares the same structure as the wing, the fuselage needs to be "ovalized" [4] in order to maintain the airfoil shape which leads to a significant reduction in the available stroke length below the passenger floor (Fig. 1). Due to

their excellent mechanical properties, GLARE laminates could provide an efficient solution for crashworthiness of unconventional aircraft. As bending is one of the major failure mechanisms that dissipate impact energy in event of a crash, this paper aims to evaluate the failure mechanism and energy absorption characteristics of GLARE laminates subjected to three-point bending loads.

Several studies have been conducted on 3-point bending of GLARE laminates. Liu et al. [5] studied the behavior of GLARE laminates subjected to short beam 3-point bending tests with the aim of determining the interlaminar shear strength of the laminates. Liu et al. [5] used GLARE-2A, GLARE-3 and GLARE-6 specimens consisting of three aluminum alloy sheets of 0.3 mm thickness and two composite layers. The authors conducted short beam bending tests for all 3 configurations, varying the span/thickness (b/h) ratio. The specimens were tested at b/h = 5,8,10 and 12. At b/h = 5, all specimens failed in a localized compression–deformation failure mode, however specimens with span/thickness ratio (b/h)≥8 were much more likely to exhibit local bending failure. For GLARE 2A and 6, Liu et al. [5] also report damage propagation to the end of the specimen for span/thickness ratio greater than 8.

Li et al. [6] studied the bending damage behavior of GLARE laminates by conducting three-point bending of GLARE-2A and GLARE-3

Nomenclature

|	
b	Span for 3-point bending tests
dx	Length of element in spring linkage model
$\dot{\delta}$	Displacement rate
ε_{max}	Strain at farthest fiber from neutral axis
h	Thickness of specimen
L	Length of specimen
ρ	Radius of curvature
ρ_{Al}	Density of aluminum
$\rho_{prepreg}$	Density of Uni-Directional (UD) prepreg
R^2	Coefficient of determination
SEA	Specific energy absorption
θ	Angle of rotation
w	Width of specimen
z_{max}	Distance of fiber farthest from the neutral axis
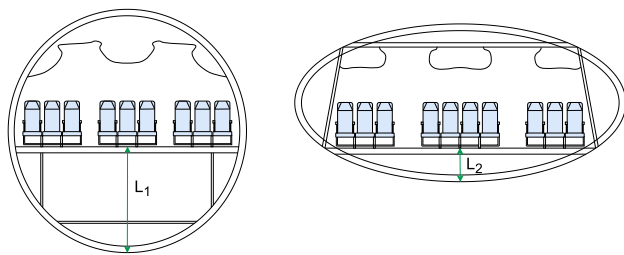
Fig. 1. Comparison between Airbus A350 (left) [9] and Flying-V fuselage cross section (right) [4].

with different layer configurations (3/2, 4/3, 5/4 and 6/5, a layer configuration of 3/2 corresponds to 3 layers of aluminum with 2 glass-fiber prepreg layers). It was observed by Li et al. [6] that loading nose radius and dimension of the specimen (length and width) have no significant effect on bending strength, however b/h ratio was shown to have significant effect on both bending strength and failure mechanism. Four failure stages were observed by Li et al. [6] for bending of GLARE laminates:

1. Stage-I: Elastic stage
2. Stage-II: Plastic stage
3. Stage-III: Local failure of fiber
4. Stage-IV: Delamination stage

Kumar et al. [7] studied the effect of aluminum layer thickness on GLARE laminates and noted a 60% increase in the load bearing capacity when the thickness is increased from 0.2 mm to 0.35 mm. Solyaev et al. [8] investigated thick GLARE laminates with varying b/h ratios under 3-point bending to determine elasto-plastic behavior and flexural strength, and also analyzed bending of GLARE specimens using a meso-scale finite element model. It was observed by Soyvalev et al. [8] that the main failure mechanism in slender specimens under bending is compression failure in the glass fiber layer followed by progressive delamination or instantaneous delamination-buckling.

The present study aims at characterizing the effect of various parameters (rolling direction, displacement rate and stacking sequence) on failure mechanism, peak load and energy absorption of GLARE laminates subjected to 3-point bending. A total of 419 specimens consisting of 5 types of GLARE are tested at varying displacement rates (1,10,100 and 1000 mm/min) and orientation (longitudinal and transverse), the number of specimens tested for each configuration is presented in Table 1.

2. Materials and methods

2.1. Material data

Five different types of GLARE (2A, 2B, 3, 4A and 4B) with varying number of layers and aluminum layer thicknesses are tested. Table 1 provides a comprehensive list of GLARE configurations, also presenting the stacking sequence, number of aluminum/prepreg layers, thicknesses and main beneficial characteristics [10] of each configuration. To aid the reader in understanding the presented data, the schematic diagrams of Fig. 2 are used to illustrate the tested orientations, and are presented as inset with the graphs. Each inset presents the laminate lay-up from the outer surface down to (but not including) the second aluminum layer. Each GLARE laminate consists of alternating aluminum and glass fiber layers, with aluminum layers on both the outermost surfaces and each glass fiber layer consisting of two prepregs [10]. The density values used for the calculations are 2.77×10^{-6} kg/mm^3 for aluminum, and 1.96×10^{-6} kg/mm^3 for glass fiber layers [11].

Material properties for S2-glass fiber/FM94 epoxy resin material and the stress–strain curve for AL2024-T3 are obtained from Hagenbeek [11], with the data presented in Table 2 and Fig. 3.

2.2. Experimental setup

For 3-point bending tests on GLARE coupons, a standard set-up (single loading pin and two supporting pins), as shown in Fig. 4, is used. The GLARE coupon is positioned on two stationary steel supporting pins, which are clamped rigidly to the mounting plate in order to eliminate any unintended lateral movement. All the pins had rounded edges with a local radius of curvature of 1.5 mm. The distance between the static supports is chosen based on the span of the coupon (b). This separation is precisely adjusted to ensure the correct span-to-thickness ratio (b/h) for each test.

The span-to-thickness ratio recommended by ASTM D790 and ASTM D7264 [12,13] is typically in the range of 16 to 60. However, in our case, the maximum separation distance between the supporting pins of the available fixtures was 60 mm, which meant that for thicker specimens a value of b/h≥16 was not possible. Due to time and cost constraints, we decided not to manufacture/procure a new fixture and instead selected a span-to-thickness ratio of 10 (b/h = 10) based on the maximum thickness observed in the tested specimens (h = 6.05 mm). A ratio of b/h = 10 is also supported by literature, where Liu et al. [5] reported that for GLARE specimens with b/h> 8, the deformation is dominated by bending. The choice of b/h = 10 ensured that all specimens could be tested at a consistent ratio across configurations. However, for some of the specimens a deviation from this value is possible due to experimental errors. The exact span of each configuration is presented in Appendix.

For thin specimens, which often exhibited folding behavior, a higher span/thickness ratio is used in order to have adequate clearance with the chamfered surface of the loading pin and for such cases b is fixed to 18 mm. Also, since the maximum separation distance of the static supports is 60 mm, the upper limit for b is fixed at 60 mm, as shown in Eq. (1). Load is applied on the test coupon at mid-span ($b/2$) with the loading pin moving downwards at four different displacement rates: 1 mm min^{-1}, 10 mm min^{-1}, 100 mm min^{-1}, and 1000 mm min^{-1}.

$$b = \begin{cases} 60 \text{ mm}, & \text{if } h > 6 \text{ mm} \\ 10 \times h, & \text{if } 1.8 \text{ mm} \le h \le 6 \text{ mm} \\ 18 \text{ mm}, & \text{if } h < 1.8 \text{ mm} \end{cases} \quad (1)$$

All samples were cut to approximately 150 mm in total length. Due to the large number of samples to be prepared, they were carefully cut with a band saw and then hand sanded to remove any burrs and edge

Table 1
Configuration of tested GLARE specimens tested.

S.No.	Type	Stacking	Main beneficial characteristics [10]	No. of layers	Aluminum layer thickness (mm)	Specimen thickness (mm)	Number of specimens tested per displacement rate (mm/min)					
							Or.	1	10	100	1000	
1	2A	0°/0°	Fatigue, strength	4/3	0.2	1.60	L	–	6	–	–	
							T	–	7	–	–	
2				4/3	0.3	2.02	L	5		–	–	
							T	5		–	–	
3				8/7	0.4	5.08	L	5	5	–	–	
							T	7	7	–	–	
4	2B	90°/90°	Fatigue, strength	7/6	0.4	4.49	L	–	–	6	5	
							T	–	–	6	5	
5				11/10	0.3	6.00	L	7	6	11	5	
							T	–	6	–	5	
6	3	0°/90°	Fatigue, impact	3/2	0.3	1.49	L	5	6	5	5	
							T	5	5	5	5	
7				5/4	0.4	2.98	L	5	5	6	5	
							T	5	5	5	6	
8				6/5	0.3	3.18	L	6	5	–	–	
							T	7	6	–	–	
9				8/7	0.4	5.19	L	5	5	5	5	
							T	6	6	–	–	
10	4A	0°/90°/0°	Fatigue, strength in 0° direction	7/6	0.4	5.20	L	9	5	5	5	
							T	5	5	5	5	
11	4B	90°/0°/90°	Fatigue, strength in 90° direction	4/3	0.4	3.01	L	–	–	7	6	
							T	–	–	6	5	
12				6/5	0.5	4.99	L	6	11	6	5	
							T	6	12	6	4	
13				7/6	0.4	5.20	L	5	5	5	5	
							T	5	5	5	5	
14				8/7	0.4	5.82	L	–	–	6	–	
							T	–	–	6	–	
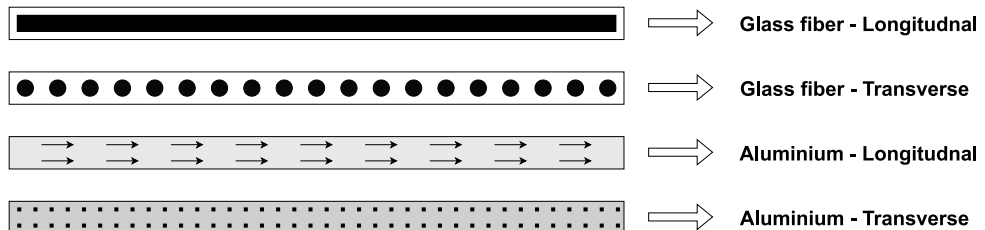
Fig. 2. Schematic diagrams for glass fiber and aluminum layers.

Table 2
Material properties for S2-glass fiber/ FM94-epoxy resin.

Orientation	Young's modulus (GPa)	Ultimate stress tensile (MPa)	Ultimate stress compressive (MPa)
Longitudinal (0°)	50.6	2273	2250
Transverse (90°)	9.9	32.54	64.87

flaws, reducing the risk of delamination initiating from the edges. The longer specimen length also served to minimize boundary condition effects in the test setup (e.g., specimen slipping out of the supports). Based on engineering judgment, 150 mm was found to be sufficiently long for reliable testing.

The 3-Point bending setup is installed on the Zwick 10kN/20kN Universal Testing Machine (UTM) [14] at the Delft Aerospace Structures and Materials Laboratory (DASML). A 20 kN Zwick load cell is used, with sampling frequencies of up to 25 Hz. A pre-load of 5 N is applied for displacement rates of 100 mm/min or higher, the pre-loading rate is always carefully matched to the test loading rate. This

approach prevented any undesired jerk motion of the loading support during pre-loading. Additionally, a sufficiently large grip separation distance is maintained to ensure the loading support moved downward at a constant vertical speed, without acceleration.

2.3. Semi-analytical model

The finite element method (FEM) is the most commonly used method to simulate 3-point bending of GLARE laminates in the literature [6,15,16]. However, such models are computationally expensive and need a more detailed geometry as starting point, being therefore not efficiently suitable as part of a preliminary design and optimization scheme. We propose a fast running semi-analytical model to predict force–displacement curves for GLARE laminates subjected to 3-point bending. The model draws its basic framework from Anand et al. [17], who focused on the bending behavior of metallic beams, combining analytical calculation of moment versus rotation curves, $M(\theta)$; with a numerical solution to assemble a spring-linkage model. The model can be best understood using the info-graphic presented in Fig. 5.

**The derivation of the $M(\theta)$ curves follows the following steps:**
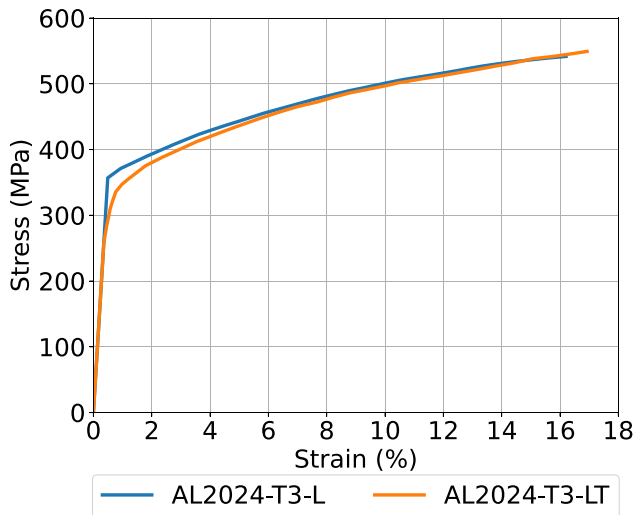
Fig. 3. True stress–strain curve for AL2024-T3 in laminated(L) and transverse(LT) directions, plotted using digitized data from [11].

1. The minimum value of radius of curvature is calculated using $\rho_{min} = z_{max}/\epsilon_{ult}$, where z_{max} is distance of farthest surface from the neutral axis. The maximum value of ρ is assumed to be a very high value $\approx 99\,999$, effectively representing an unbent hybrid laminate. The algorithm then iterates from ρ_{min} to ρ_{max}.

2. For a given ρ:

   (a) A linear strain distribution across the cross-section is assumed with $\epsilon = 0$ at neutral axis and $\epsilon = z_{max}/\rho$ at fiber farthest from the neutral axis.

   (b) A stress distribution is calculated from the strain distribution using a direct lookup on stress–strain curves from aluminum or glass fiber laminate coupons. For aluminum, there is coupon data for laminated and transverse directions; whereas for glass fibers there is coupon data for each fiber orientation herein adopted, i.e. 0°, ±45° or 90°.

   (c) The moment is calculated from the stress distribution, and the corresponding θ is calculated from the equation $\theta = dx/\rho$.

   (d) Due to the plastic behavior of aluminum, for the aluminum layers the strain distribution is converted to true strain using $\sigma_{true} = ln(1 + \varepsilon_{eng})$, the lookup is then performed using true stress–strain curves, with the area used for the moment calculation adjusted using $Area = A_0/(1 + \varepsilon_{eng})$.

3. Step 2 is repeated for all values of ρ to assemble the $M(\theta)$ curve. The moment at which a transverse fracture of a layer occurs is recorded along with the information of the layer which fails.

Spring-linkage model: In the spring-linkage model, the beam is assumed to be divided into very small rigid elements of length dx. These rigid elements are interconnected using torsional springs. The calculation of the force–displacement curve then follows the steps enumerated below:

1. For a given configuration, the neutral axis is calculated using all the undamaged layers assuming elastic young's modulus for each layer.

2. Based on the calculated position of neutral axis, the moment-theta relationship is calculated following the methodology outlined earlier.

3. A ramp force is then applied to a cantilever beam, varying from 0 to F_{max}.

4. At each time step, a moment is calculated on all the springs by estimating the lever arm and based on the applied moment, rotation for each spring is calculated.

5. Based on the calculated rotation, the new position of each rigid element is calculated and the tip displacement is estimated.

6. The point is added to the force versus displacement curve, since the experimental studies are conducted using 3-point bending, the force values from the python model are doubled as the spring-linkage model uses a cantilever beam.

7. If no additional transverse fracture of a layer occurs, the algorithm loops back and repeats the steps. If, instead, the moment reaches the value that triggers transverse failure in any layer (Step 4), the simulation halts. The affected layer is flagged as damaged, the Moment-versus-theta curve is rebuilt taking all existing failed layers into account and the analysis restarts from $t = 0$.

After all the force-versus displacement curves are obtained, they are assembled together to get the complete force versus displacement response. From the first run (undamaged laminate), Force-versus-displacement from 0 to $F_{failure-1}$ is considered. Then from the second run (1 layer damaged) Force-versus-displacement from $F_{failure-1}$ (Force at which failure occurs in 1st run) to $F_{failure-2}$ (Force at which transverse failure of a layer occurs in 2nd run) is considered. A vertical drop is assumed between the curves, and is shown by vertical dotted lines in Fig. 6.

Assumptions and limitations for the semi-analytical model:

1. Only quasi-static loading is considered; rate effects have not been included.

2. Perfect bonding is assumed between the layers.

3. Shear effects are neglected. *Note:* An energy based shear correction routine is implemented in the model. Users can enable shear correction by adjusting a variable (Capture_shear). Minimal impact on the results was observed for the cases considered in this study. It is important to note that the results for shear have not been verified or validated. However, the implemented algorithm for the model included in the dataset contains the shear correction routine as part of the code for future verification, correction or extension by other researchers.

4. The model does not account for slippage over the supporting pins, consequently the span remains constant.

5. Delamination mechanics or mixed mode failure are not modeled.

6. Partial degradation of the ply is not considered, a ply is marked as failed only when the entire ply exceeds the strain limit.

7. Geometric non-linearity is ignored, except for plastic thinning in aluminum layers.

3. Results

3.1. Experimental results

Appendix A.5 reports the specific energy absorption (SEA) (kJ/kg), peak force (kN), and bending modulus (GPa) for all GLARE configurations. A more detailed dataset containing all the experimentally collected data, curves, and images can be found in the public dataset of Anand et al. [18].

The equations used for the calculation of SEA and bending modulus are enumerated below:

1. SEA (kJ/kg): the energy absorbed per unit mass of the laminate, calculated as:

$$SEA = \frac{\text{Energy absorbed}}{M} \tag{2}$$

where M is the mass of the specimen calculated using:

$$M = n_{Al} \cdot \rho_{Al} \cdot (L \cdot w \cdot h_{Al}) + n_{prepreg} \cdot \rho_{prepreg} \cdot (L \cdot w \cdot h_{prepreg}) \tag{3}$$

with:

(a) Actual

(b) Schematic
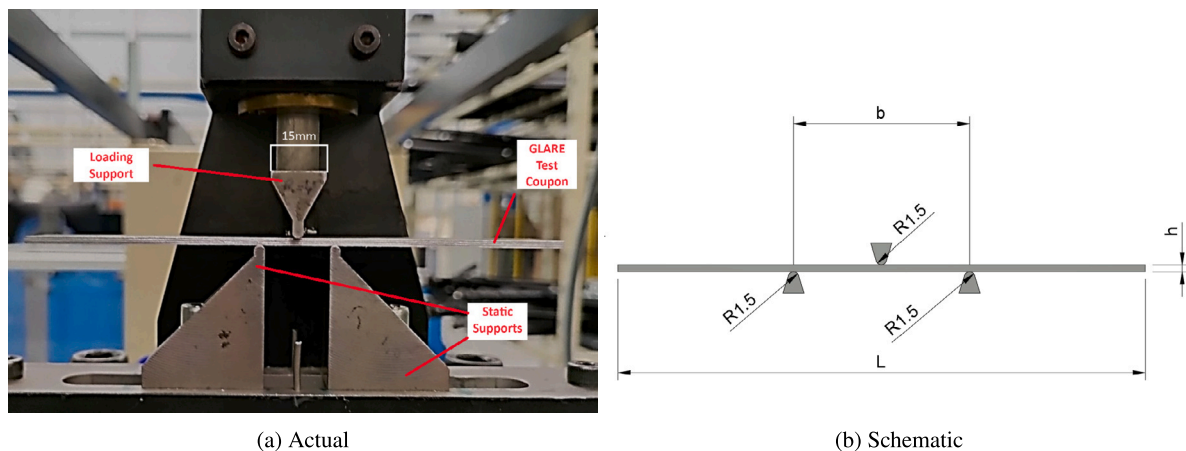
Fig. 4. 3-Point bending test setup.
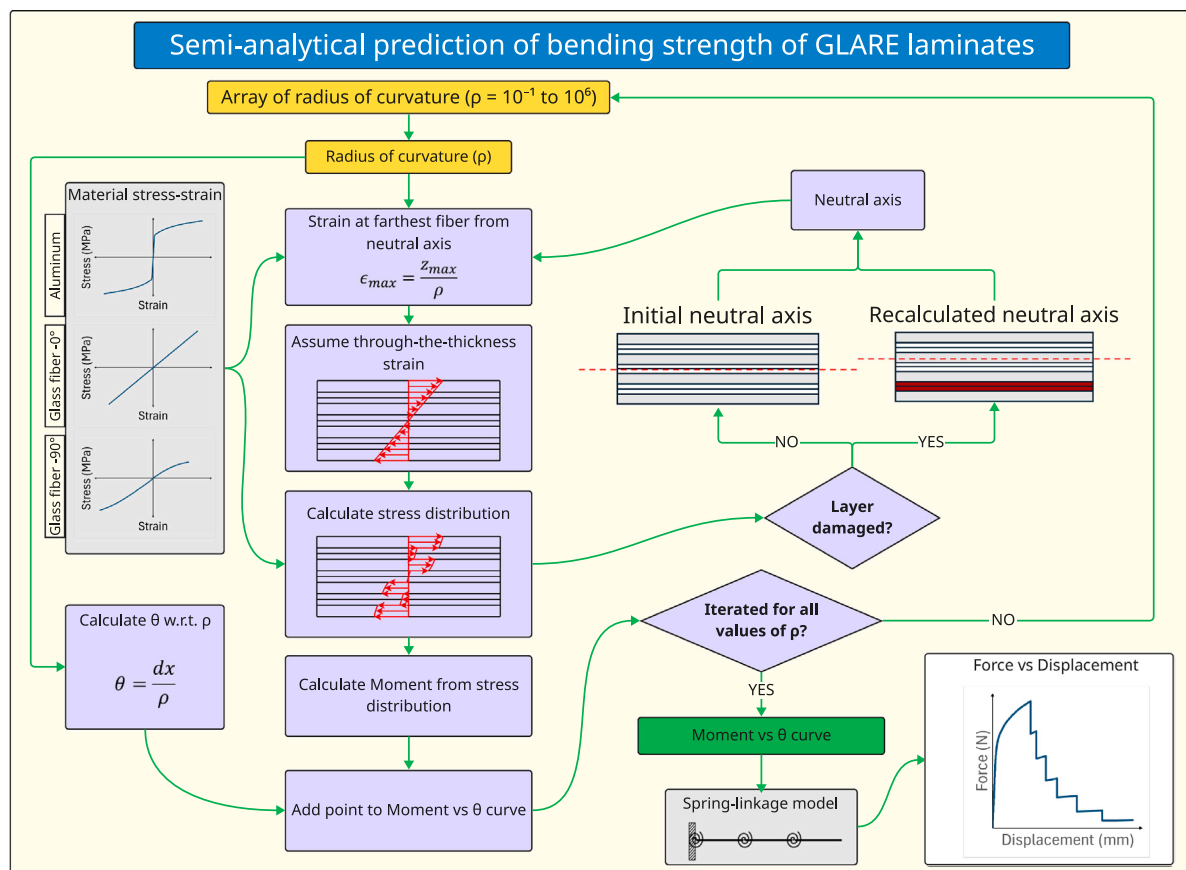
Fig. 5. Infographic: Semi-analytical prediction of bending strength of GLARE laminates.

n_{Al} = Number of aluminum layers
$n_{prepreg}$ = Number of glass fiber layers
h_{Al} = Thickness of aluminum layers
$h_{prepreg}$ = Thickness of glass fiber layers
ρ_{Al} = Density of aluminum (2.77×10^{-6} kg/mm^3) [11]
$\rho_{prepreg}$ = Density of UD prepreg (1.96×10^{-6} kg/mm^3) [11]
L = Length of the specimen
w = Width

It is important to note that Specific Energy Absorption (SEA) values reported in this study are calculated based on the total length of the specimen, which is constant across all specimens (≈ 150 mm), to ensure consistent comparison across the tested laminates. However, the damaged region can vary considerably between specimens, for example only the mid-span region is damaged for central cracking cases while the region from mid-span to end of the sample is damaged for delamination cases. Therefore, the reported SEA values should be interpreted with caution. While the values should not be interpreted as a direct measure of energy absorption efficiency of the damaged region, they provide a consistent basis for comparing the relative energy absorption capability of tested GLARE configurations.
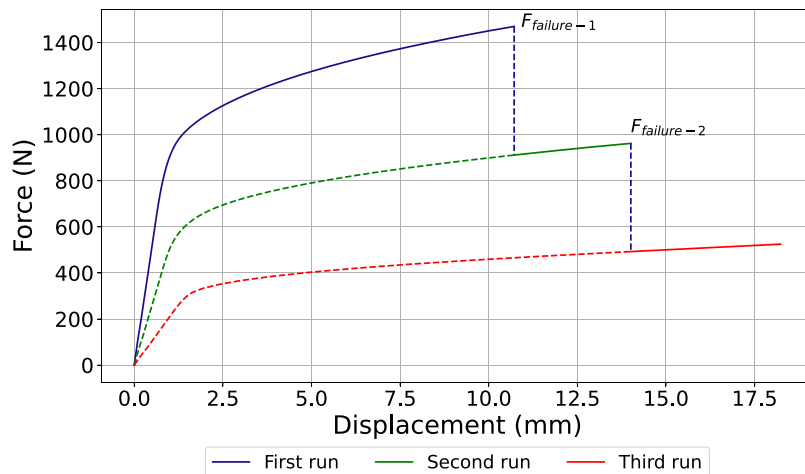
Fig. 6. Example force versus displacement curve with vertical drops after transverse failure of layers indicated with dotted lines.

2. Bending modulus (GPa): the material's stiffness under bending load, calculated as:

$$E_{flex} = \frac{m_{elastic} \cdot b^3}{4 \cdot w \cdot h^3} \tag{4}$$

where:

$m_{elastic}$ = Slope for elastic region of force versus displacement curve
b = Span
w = Width
h = Thickness

The slope for elastic region ($m_{elastic}$) was calculated by using an automated script. The script imports force versus displacement curve, applies toe compensation of 2.5% peak force, and then extracts the portion of curve from zero displacement to displacement corresponding to peak force. This extracted segment is then interpolated using a denser set of points to ensure a smooth curve. Subsequently, linear regression over the region corresponding to 20%–30% (except for the very thin case : 2A-4/3-[L&T]-0.2 (10 mm/min), where the window used was 10 to 30% of peak force) of peak force is performed with an (R^2) threshold of greater than 0.98 to ensure accurate value of slope for elastic region.

Some example curves for experimental 3 point bending are presented in Fig. 7, the effect of different parameters on the energy absorption and other characteristics are discussed in Section 4.

3.2. Repeatability of experimental results

To assess the repeatability of experimental data the following methodology was used:

1. First, a toe compensation of 2.5% of the peak force was applied to all experimentally obtained force-versus-displacement curves to remove the initial non-linear region.
2. For each GLARE configuration:

   (a) The minimum of the maximum displacements observed across all samples was identified. A displacement array was then defined from 0 to this identified displacement value, consisting of 500 equally spaced points.
   (b) The force–displacement curves for all the samples of that GLARE configuration was then mapped to this common displacement array ensuring standardized force–displacement curves across samples.

   (c) The mean force–displacement curve was calculated as point-wise average of the interpolated curves.
   (d) All the curves for the given configuration were then normalized, the displacement axis by dividing the common displacement array with maximum displacement value and the force axis by dividing with peak force of the mean force–displacement curve.
   (e) For each sample the area between its normalized curve and the normalized mean curve was calculated.
   (f) Finally for any given GLARE configuration, we obtain a list containing area between the normalized mean curve and the normalized sample curves. The minimum, maximum and mean of this list is then calculated.

Fig. 8 plots the minimum, maximum and mean values of the area between normalized experimental curves and normalized mean curve observed for the tested configurations. The mean area between the curves was found to be always below 0.09 for all configurations, demonstrating that the experiments are repeatable. Repeatability of experimental data can also be observed from the graphs presented in Appendix A.6.

3.3. Results from semi-analytical model for central cracking

The comparison of curves from the semi-analytical model with the experimental results are presented in Appendix A.6 with only two example curves presented here, Fig. 9. The predictions of the model were found to be significantly close to experimentally observed results and have been further discussed in Section 4.5.

4. Discussion

The discussion is organized into the following sub-sections:

4.1 Failure mechanisms
4.2 Effect of stacking sequence
4.3 Effect of displacement rate
4.4 Effect of aluminum rolling direction
4.5 Results from semi-analytical model
4.6 Sensitivity of force–displacement curve to span

4.1. Failure mechanisms

From the experimental results, four failure mechanisms were observed (Fig. 10) through which GLARE laminates fail when subjected to 3-point bending loads. These mechanisms are divided into two categories, normal stress dominated failure and shear stress dominated failure.

(a) 2A-8/7-L-0.4 Sample-2 (1 mm/min)

(b) 2B-11/10-L-0.3 Sample-3 (10 mm/min)

(c) 3-3/2-L-0.3 Sample-4 (100 mm/min)

(d) 4B-6/5-T-0.5 Sample-3 (1000 mm/min)
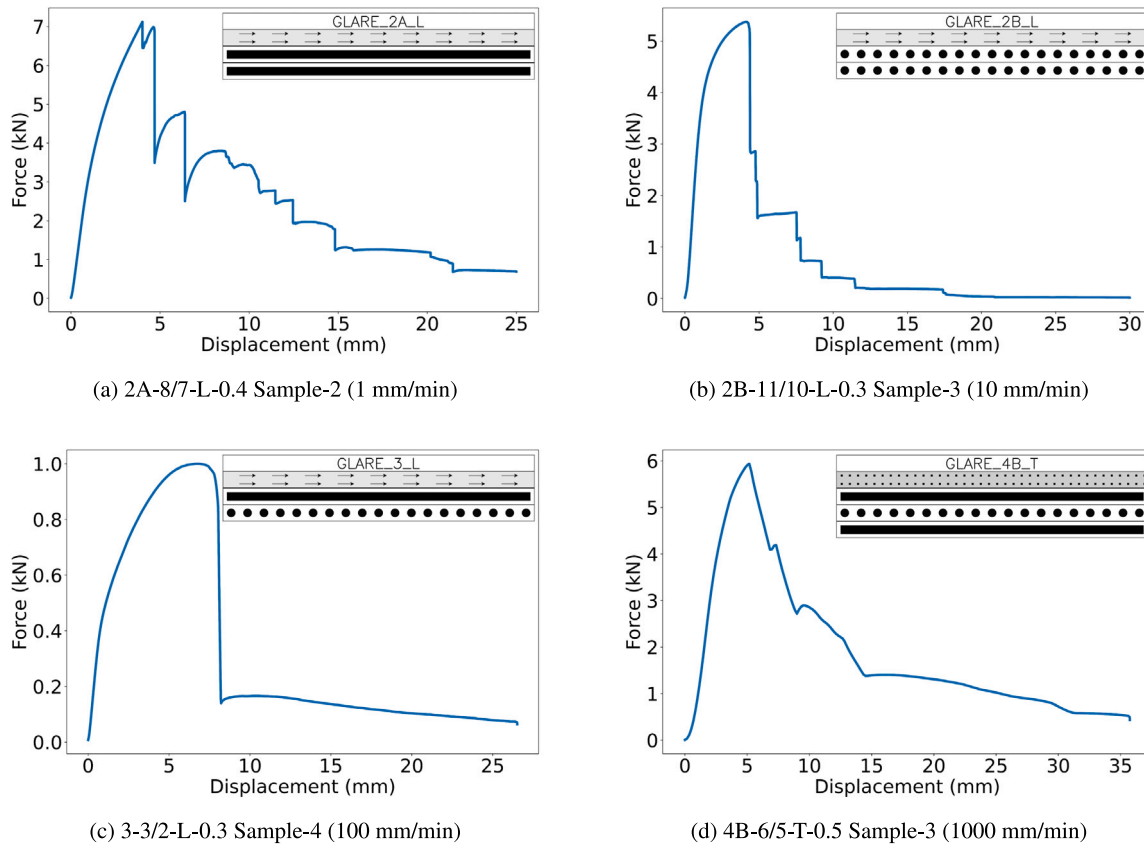
Fig. 7. Experimental force versus displacement for GLARE laminates subjected to 3-point bending.
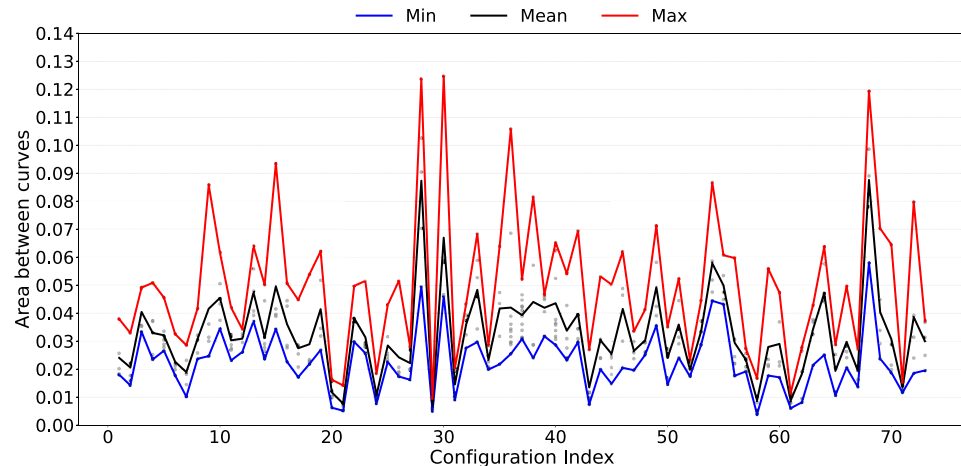

Fig. 8. Minimum, mean and maximum area between curves versus configuration for normalized experimental dataset.

1. **Normal stress dominated failure mechanisms:**

   (a) **Central Cracking (CC):**
   In this failure mechanism the outermost aluminum ply fractures due to an increase in tensile stress and the crack slowly progresses toward the inner layer as the laminate is loaded further. During progressive failure under bending, the local mid-surface progressively moves to the innermost ply, thus allowing tensile stresses that can grow the central crack to reach those inner plies. This failure mechanism was observed in laminates where most of glass fiber plies have a 90° orientation.

2. **Shear dominated failure mechanisms**

   (a) **Delamination (D):**
   This failure mode is transverse-shear dominated, with the delamination crack initiating near the neutral axis, where the transverse shear is maximum, and then growing longitudinally all the way to the end due to the transverse shear loading. A specimen can have single or multiple delaminations (Figs. 10(b) and 10(c)). This failure mode is observed in laminates which have most of glass fiber plies in 0° orientation, which are more prone to transverse-shear driven failure due to high tensile and compressive failure stresses.
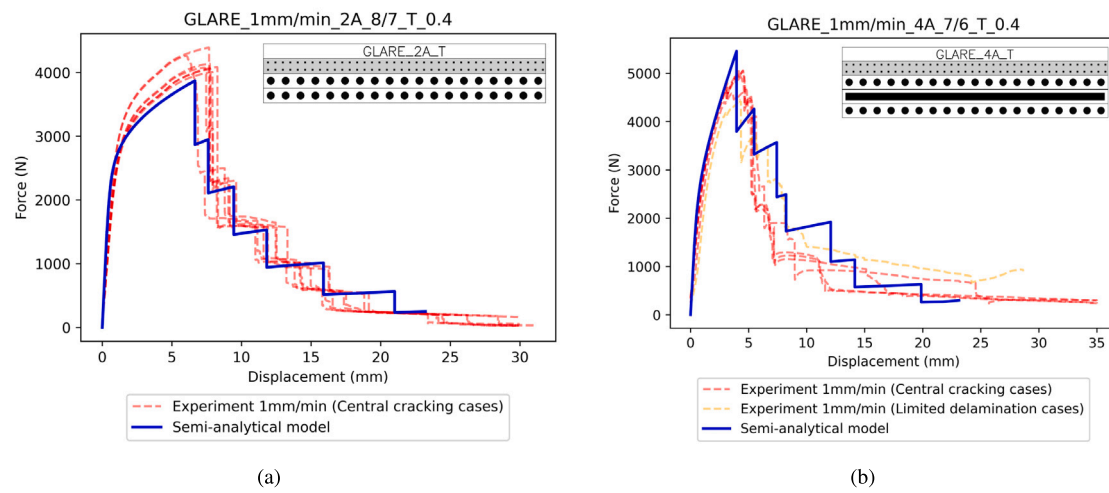
(a)   (b)

Fig. 9. Comparison of experimental force-versus-displacement curves with predictions from semi-analytical model.

(a) Central cracking   (b) Delamination

(c) Delamination (multiple)   (d) Limited Delamination
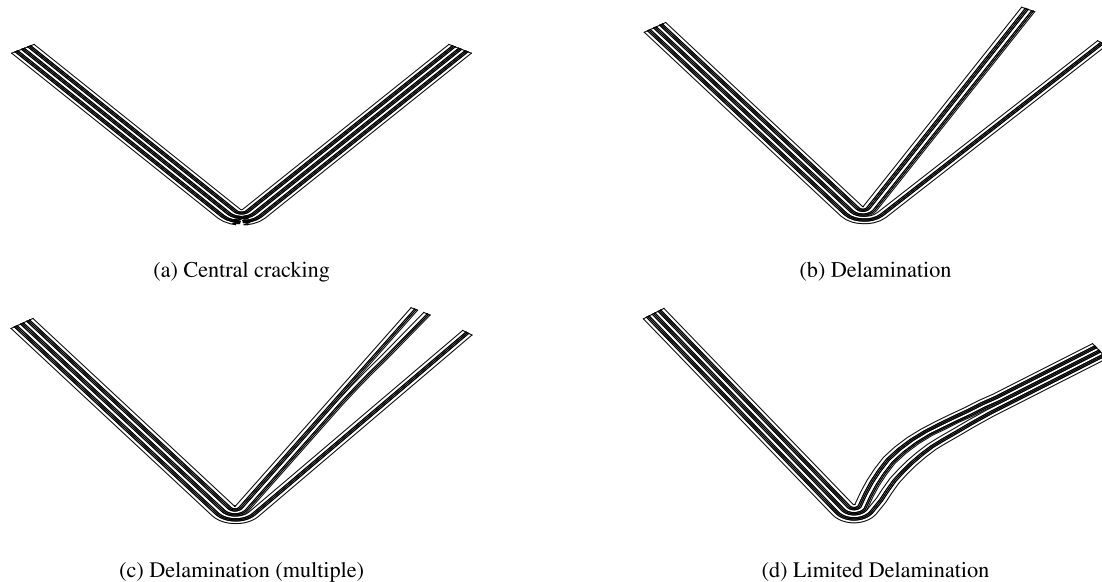
Fig. 10. Failure modes observed GLARE laminates subjected to 3 point bending.

(b) **Limited Delamination (LD):**

This failure mode is triggered similarly to the delamination failure mode; however, limited delamination does not progress all the way to the end of the specimen. A specimen can have single or multiple localized delaminations. Observed in laminates which have majority of glass plies in 0° orientation.

The failure modes observed for different configurations at different displacement rates are presented in Tables 3–5. Typical force versus displacement curves for different failure mechanisms are presented in Figs. 11 and 12 along with images of the damaged specimens taken after testing. For laminates with all glass fiber plies in 90° direction, it is observed (Fig. 11(a)) that the abrupt load drops for central cracking, resulting from failure of aluminum layers, are immediately followed by a plateau, a response consistent with plastic hinge formation in aluminum. For central cracking cases where the laminate has some glass fiber plies in 0° direction, similar load drops can be caused by failure of aluminum layers or failure of 0° glass fiber layers. When some aluminum and 0° glass fiber layers are still intact, a small rise in load generally follows this drop. However, at higher displacements (i.e., further along the force–displacement curve), plateaus can be observed to follow the drop indicating that the plastic bending of aluminum layers governs the residual flexural resistance.

For the shear dominated cases (Figs. 12(a) and 12(b)), multiple peaks and drops were observed which correspond to a combination of delamination and transverse failure of aluminum or 0° glass fiber layers. In most samples that delaminated, the bottom aluminum layer fractured transversely with further loading of the specimen after delamination.

4.2. Effect of stacking sequence

Fig. 13 presents the effect of stacking sequence on failure mechanism and specific energy absorption (SEA). From the results several observations can be made with respect to stacking sequence:

1. **Configurations where glass fiber layers are only in 90° (transverse) direction, 2A-T and 2B-L:** As illustrated in Fig. 13, both configurations 2A-T and 2B-L failed through central cracking mechanism for all tested specimens. With increasing applied force, matrix cracking initiates in the 90° fiber layers due to the relatively low failure stress of the matrix. This is subsequently followed by yielding and tensile failure of the
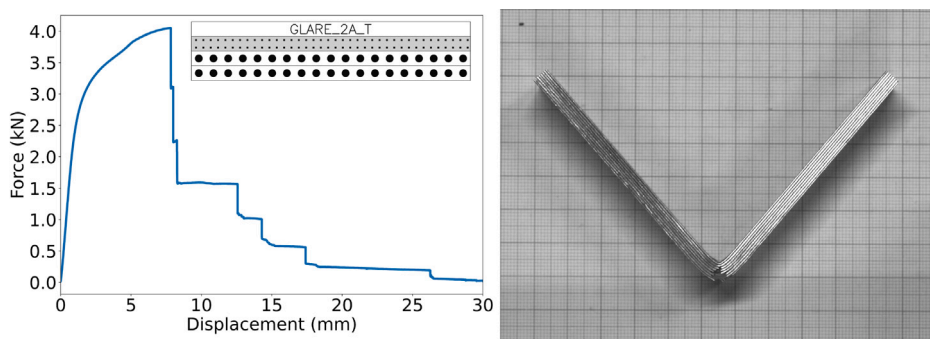
(a) Central cracking failure: GLARE-2A-8/7-T-0.4 Sample 5
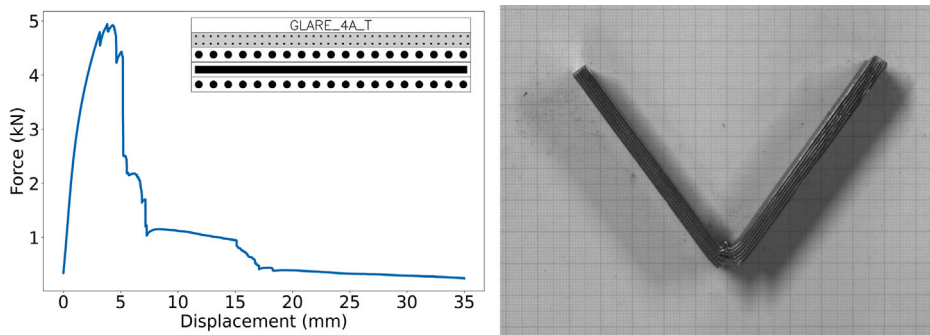
(b) Central cracking failure: GLARE-4A-7/6-T-0.4 Sample 1

Fig. 11. Typical force versus displacement curves for central-cracking failure mechanisms.
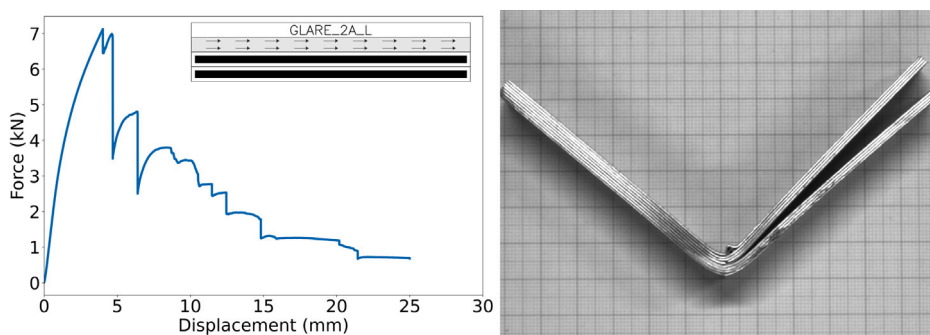
(a) Delamination failure: GLARE-2A-8/7-L-0.4 Sample 2
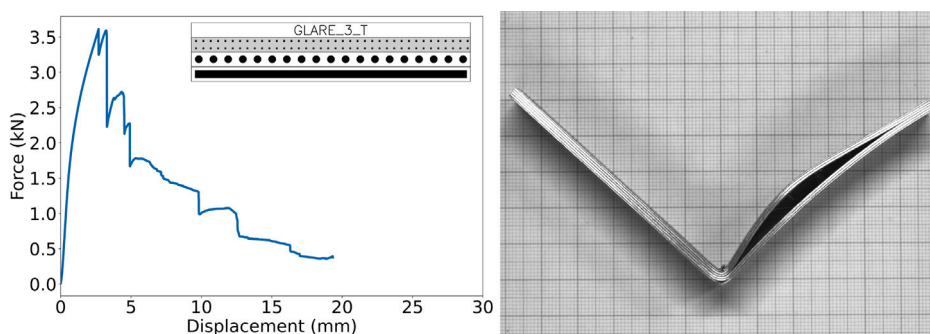
(b) Limited delamination failure: GLARE-3-6/5-T-0.3 Sample 4

Fig. 12. Typical force versus displacement curves for shear dominated failure mechanisms.

Table 3

Failure modes observed for GLARE-2 specimens.

Configuration	$\dot{\delta}$ (mm/min)	Observed failure modes			Configuration	$\dot{\delta}$ (mm/min)	Observed failure modes		
		CC	D	LD			CC	D	LD
2A_4/3_L_0.3	1	–	–	5	2B_7/6_L_0.4	100	6	–	–
2A_4/3_T_0.3	1	5	–	–		1000	5	–	–
2A_4/3_L_0.2	10	–	–	6	2B_7/6_T_0.4	100	–	6	–
2A_4/3_T_0.2	10	7	–	–		1000	–	5	–
2A_8/7_L_0.4	1	–	5	–	2B_11/10_L_0.3	1	7	–	–
	10	–	5	–		10	6	–	–
2A_8/7_T_0.4	1	7	–	–		100	11	–	–
	10	7	–	–		1000	5	–	–
-					2B_11/10_T_0.3	10	–	6	–

Table 4

Failure modes observed for GLARE-3 specimens.

Configuration	$\dot{\delta}$ (mm/min)	Observed failure modes			Configuration	$\dot{\delta}$ (mm/min)	Observed failure modes		
		CC	D	LD			CC	D	LD
3_3/2_L_0.3	1	5	–	–	3_5/4_T_0.4	10	5	–	–
	10	6	–	–		100	–	3	2
	100	5	–	–		1000	2	3	1
	1000	5	–	–	3_6/5_L_0.3	1	–	–	6
3_3/2_T_0.3	1	5	–	–		10	3	–	2
	10	5	–	–	3_6/5_T_0.3	1	–	–	7
	100	5	–	–		10	6	–	–
	1000	5	–	–	3_8/7_L_0.4	1	–	5	–
3_5/4_L_0.4	1	–	–	5		10	–	5	–
	10	–	–	5		100	5	–	–
	100	–	6	–		1000	5	–	–
	1000	–	5	–	3_8/7_T_0.4	1	1	5	–
3_5/4_T_0.4	1	–	–	5		10	2	4	–

Table 5

Failure modes observed for GLARE-4 specimens.

Configuration	$\dot{\delta}$ (mm/min)	Observed failure modes			Configuration	$\dot{\delta}$ (mm/min)	Observed failure modes		
		CC	D	LD			CC	D	LD
4A_7/6_L_0.4	1	–	9	–	4B_6/5_L_0.5	1000	5	–	–
	10	–	5	–	4B_6/5_T_0.5	1	–	–	6
	100	–	5	–		10	–	12	–
	1000	–	5	–		100	–	6	–
4A_7/6_T_0.4	1	4	–	1		1000	–	4	–
	10	4	–	1	4B_7/6_L_0.4	1	1	4	–
	100	4	1	–		10	1	4	–
	1000	5	–	–		100	3	1	1
4B_4/3_L_0.4	100	7	–	–		1000	4	1	–
	1000	3	–	3	4B_7/6_T_0.4	1	–	4	1
4B_4/3_T_0.4	100	6	–	–		10	–	5	–
	1000	–	4	1		100	–	5	–
4B_6/5_L_0.5	1	–	–	6		1000	–	4	1
	10	9	2	–	4B_8/7_L_0.4	100	5	1	–
	100	6	–	–	4B_8/7_T_0.4	100	–	6	–

aluminum layers, leading to the formation of a central crack propagating upward from the bottommost layer. The average SEA for these specimens is found to be 0.69 kJ/kg. Minimum average SEA value of 0.09 kJ/kg was observed for 2A-4/3-T-0.2 specimens tested at a displacement rate of 10 mm/min and maximum average SEA value of 1.03 kJ/kg was observed for 2A-8/7-T-0.4 specimens tested at a displacement rate of 10 mm/min. (Fig. 20).

2. **Configurations where glass fiber layers are only in 0° (longitudinal) direction, 2A-L and 2B-T:** Configurations 2A-L and 2B-T, both display shear dominated failure mechanisms. For these

stacking sequences, as the force increases, the aluminum layers start yielding which causes a change in slope of the force versus displacement curve. Given the relative high strength of glass fibers in the longitudinal direction as compared to transverse direction (Table 2), further increase in force leads to a shear dominated failure as opposed to central cracking failure observed in configurations with 90° fiber layers. As shown in Fig. 13, all the specimens of configurations 2A-L and 2B-T failed through shear dominated failure (delamination and limited delamination). The recorded SEA values for 2A-L and 2B-T configurations are significantly higher than the configurations with all fiber
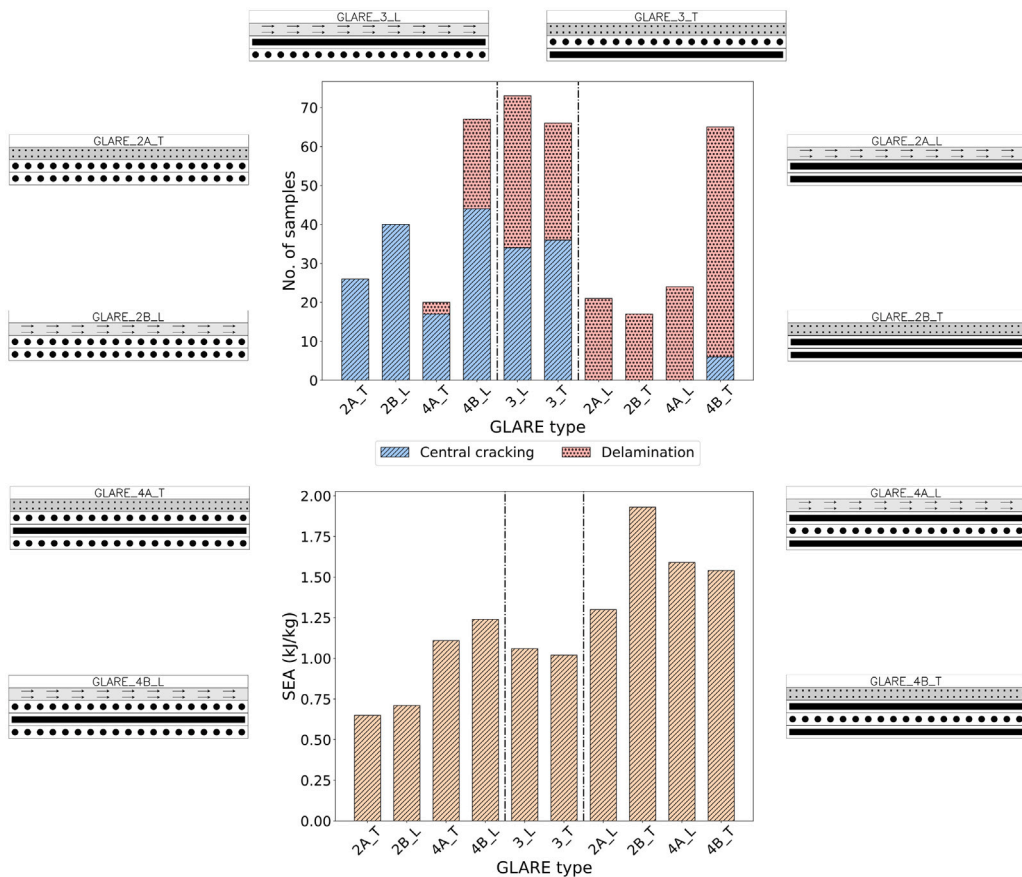
Fig. 13. Effect of stacking sequence on failure mode and specific energy absorption (SEA).
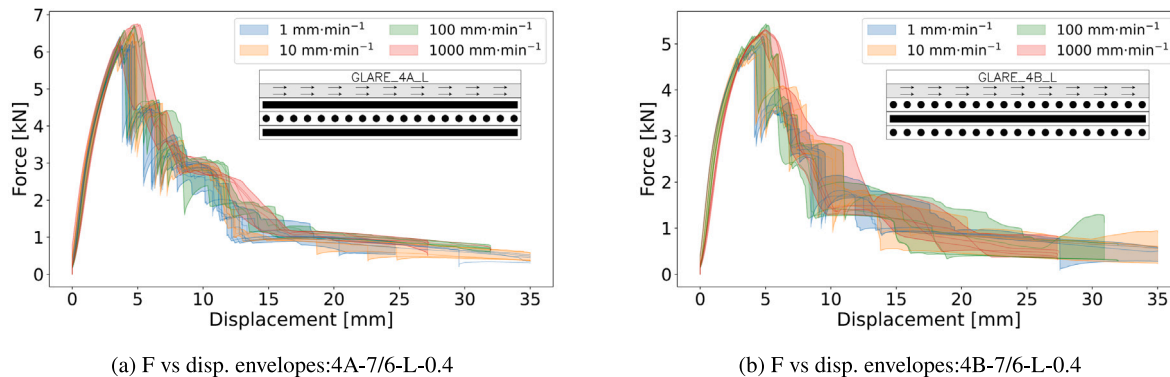
(a) F vs disp. envelopes:4A-7/6-L-0.4

(b) F vs disp. envelopes:4B-7/6-L-0.4

Fig. 14. Comparison of experimental force-versus-displacement envelopes for specimens with change in displacement rate.

layers in the 90° direction. Average SEA for the configurations 2A-4/3-L-0.2 and 2A-4/3-L-0.3, which are relatively thin, was recorded to be 1.06 kJ/kg and 0.87 kJ/kg respectively. As shown in Fig. 20, the average SEA for the other thicker configurations is recorded to be 1.83 kJ/kg with minimum and maximum values being 1.52 kJ/kg (2A-8/7-L-0.4-Sample-5, tested at 1 mm/min) and 2.22 kJ/kg (2B-7/6-T-0.4-Sample-5, tested at 1000 mm/min) respectively.

3. **Configurations with a 1:1 ratio between fibers in 90° (transverse) and 0° (longitudinal) direction, 3-L and 3-T:** Such configurations generally show a mix of central cracking and shear dominated failure modes (Fig. 13), except for very thin configurations (3-3/2-L-0.3 and 3-3/2-T-0.3) which show central cracking followed by folding for all the 4 displacement rates (1 mm/min, 10 mm/min, 100 mm/min and 1000 mm/min).

The average SEA value for GLARE-3 configurations is 1.04 kJ/kg, with minimum and maximum recorded values being 0.57 kJ/kg and 1.81 kJ/kg, also illustrated in Fig. 21.

4. **Configurations with a 2:1 ratio between fibers in 0° (longitudinal) and 90° (transverse) direction, 4A-L and 4B-T:** Configurations 4A-L and 4B-T, with a stacking orientation of 0°/90°/0°, 6 out of 89 total cases failed with central cracking failure, while the rest 83 showed shear dominated failure. This can be observed for the following cases: 4A-7/6-L-0.4, 4B-4/3-T-0.4, 4B-6/5-T-0.5, 4B-7/6-T-0.4 and 4B-8/7-T-0.4. The average SEA value for configurations 4A-L and 4B-T is 1.56 kJ/kg, with a minimum of 1.07 kJ/kg and a maximum of 1.88 kJ/kg, as shown in Fig. 22.

For the configuration 4B-4/3-T-0.4, all six specimens tested at a displacement rate of 100 mm/min exhibited central cracking
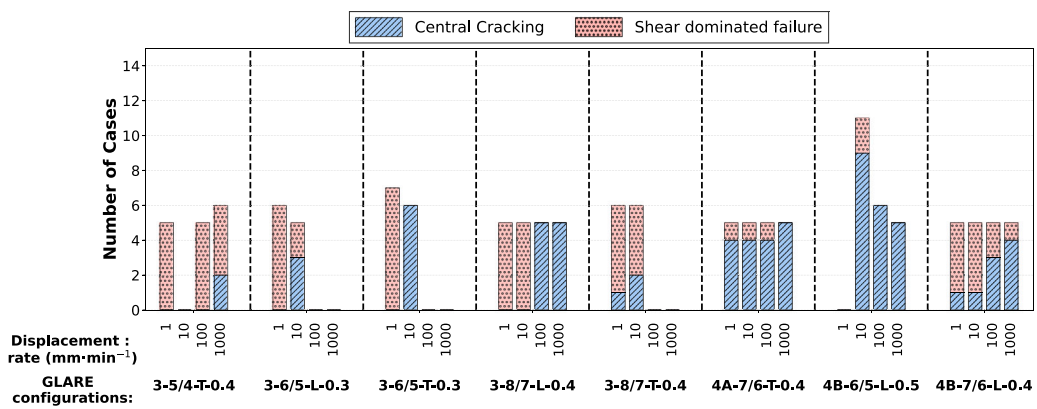
Fig. 15. Effect of displacement rate on failure modes.
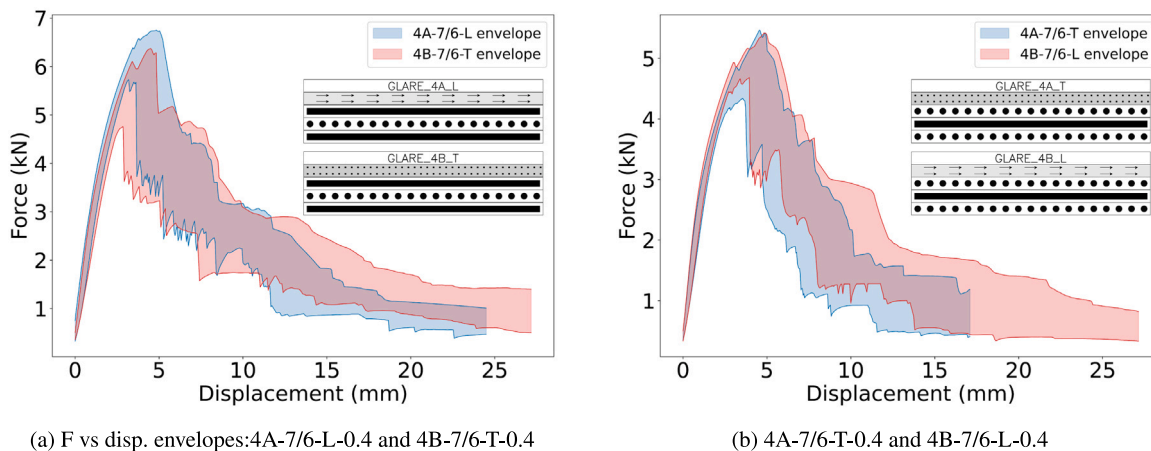
(a) F vs disp. envelopes:4A-7/6-L-0.4 and 4B-7/6-T-0.4

(b) 4A-7/6-T-0.4 and 4B-7/6-L-0.4

Fig. 16. Comparison of experimental force-versus-displacement envelopes for specimens with change in aluminum rolling direction.

failure. However, these specimens were inadvertently tested at a span-to-thickness (b/h) ratio of 20, instead of the standard value of 10. This higher span-to-thickness ratio reduces the transverse shear stress component relative to the bending moment, thereby favoring normal stress dominated failure mechanism.

5. **Configurations with a 2:1 ratio between fibers in 90° (transverse) and 0° (longitudinal) direction, 4A-T and 4B-L:** The cases 4A-T and 4B-L, with a stacking orientation of 90°/0°/90°, tend to usually fail by central cracking, however a substantial amount of specimens also failed through shear dominated failure. 61 out of a total 87 specimens tested failed through central cracking while the rest of the specimens failed through shear dominated failure mechanisms (delamination and limited delamination). Various 4A-T and 4B-L cases are presented below:

   (a) **4A-7/6-T-0.4** (Central cracking: 17 specimens, Shear dominated failure:3 specimens)
   Delamination for 1 specimen at 100 mm/min and limited delamination for 1 specimen each is observed for 1 and 10 mm/min, the peak force and SEA for these specimens with shear dominated failure was found to be in the same range (Peak force range: 4.45 to 4.73 kN, SEA range: 0.91 to 1.37 kJ/kg) as other specimens that failed through central cracking (peak force range: 4.49 to 5.47 kN, SEA range: 0.97 to 1.30 kJ/kg) indicating that the energy required for these failure mechanisms are similar.

   (b) **4B-8/7-L-0.4** (Central cracking: 5 specimens, Shear dominated failure:1 specimens)
   GLARE-4B-8/7-L specimens are only tested at 100 mm/min due to lack of material of this type, for 6 tested specimens,

5 failed through central cracking and delamination was observed for 1 case. The peak force was observed to be about 5.7% lower for delamination case (6.09 kN) as compared to peak force for central cracking cases (Average peak force = 6.46 kN), while SEA for delamination failure was found to be higher (1.51 kJ/kg) than for central cracking failure (Average SEA = 1.24 kJ/kg).

   (c) **4B-4/3-L-0.4** (Central cracking: 10 specimens, Shear dominated failure:3 specimens)
   The specimens for 4B-4/3-L-0.4 were inadvertently tested at two different spans for 100 and 1000 mm displacement rates, with specimens for 100 mm/min tested at b/h ratio of 20 instead of 10, while specimens for 1000 mm/min were tested at b/h ratio of 12. 3 specimens tested at 1000 mm/min displacement rate failed through central cracking mechanism while rest 3 fail through limited delamination failure. However, all specimens tested at a 100 mm/min displacement rate and higher span ($b/h = 20$) failed through central cracking.

   (d) **4B-6/5-L-0.5** (Central cracking: 20 specimens, Shear dominated failure:8 specimens)
   For 1 mm/min displacement rate, all specimens showed limited delamination failure; however, there is an error in the span for these specimens and from the results it is evident that these specimens were tested at a b/h ratio significantly lesser than 10. Between the rest 22 specimens tested at displacement rates of 10, 100 and 1000 mm/min, 2 at 10 mm/min failed through delamination, while the rest of the specimens failed through central cracking.
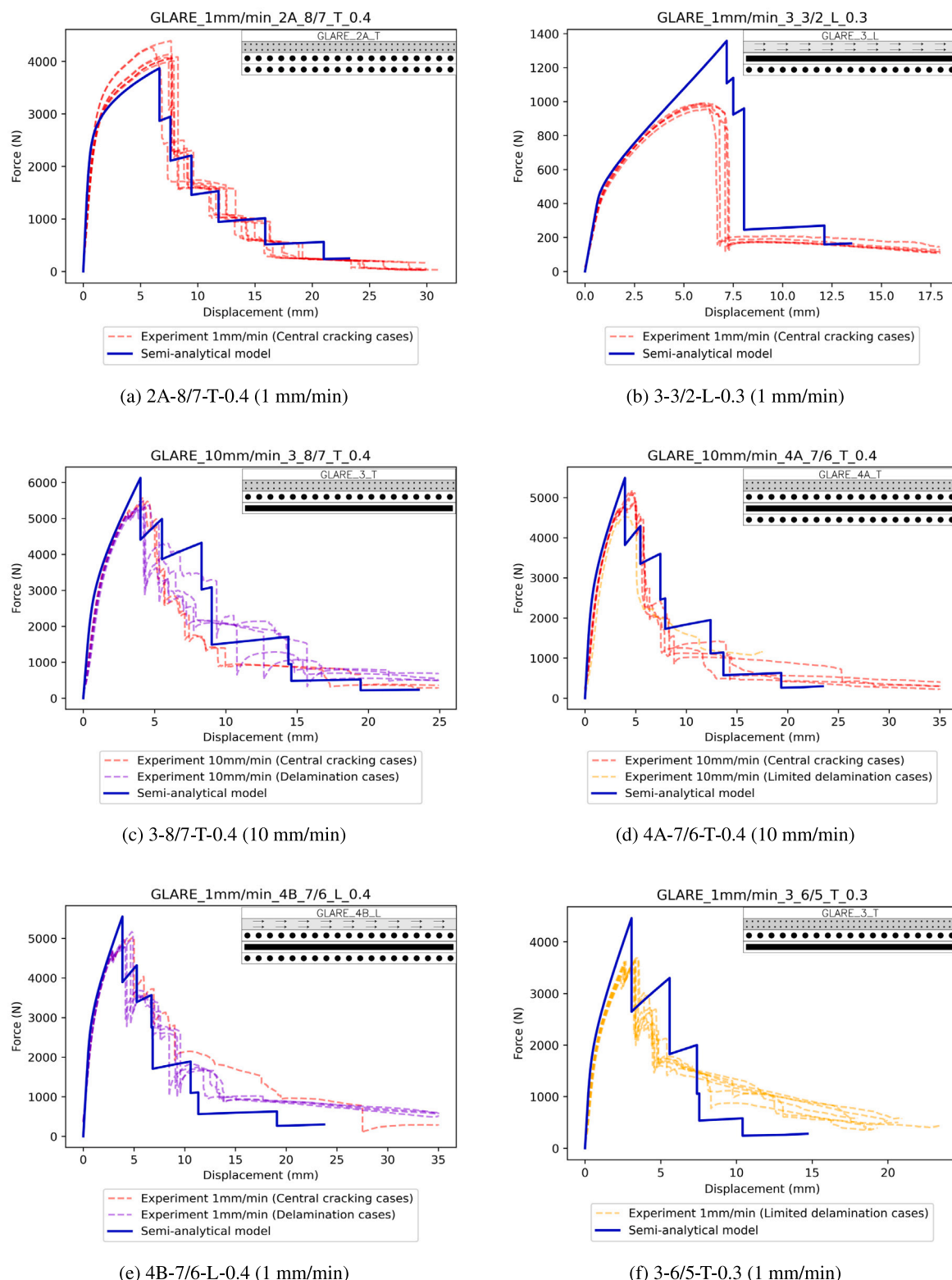
Fig. 17. Comparison of experimental force-versus-displacement curves with predictions from semi-analytical model.

(e) **4B-7/6-L-0.4** (Central cracking: 9 specimens, Shear dominated failure:11 specimens)

For all displacement rates a combination of central cracking and shear dominated failure is observed with the number of specimens showing central cracking increasing with an increase in displacement rate. Among the specimens with shear dominated failure, 1 specimen showed

limited delamination failure and rest showed delamination failure. The average peak force is a bit lower, while the average SEA is higher for shear dominated failure cases. (Central cracking failure: average peak force = 5.29 kN, average SEA= 1.26 kJ/kg and shear dominated failure: average peak force = 4.95 kN, average SEA = 1.47 kJ/kg).
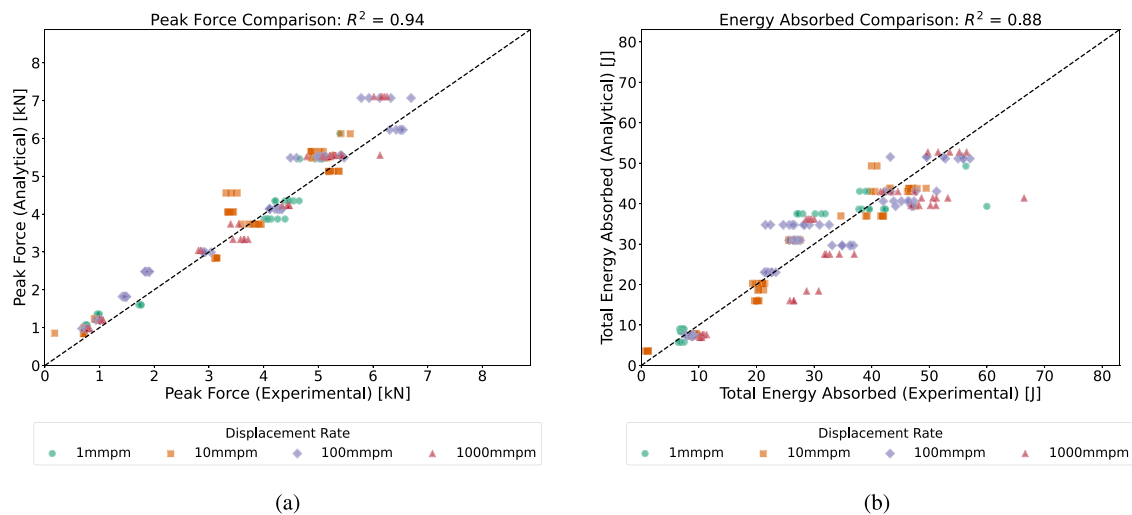
Fig. 18. Comparison of analytical and experimental values for peak force and total energy absorbed, only central cracking cases are considered. Dotted lines represent ideal correlation, experimental = analytical.
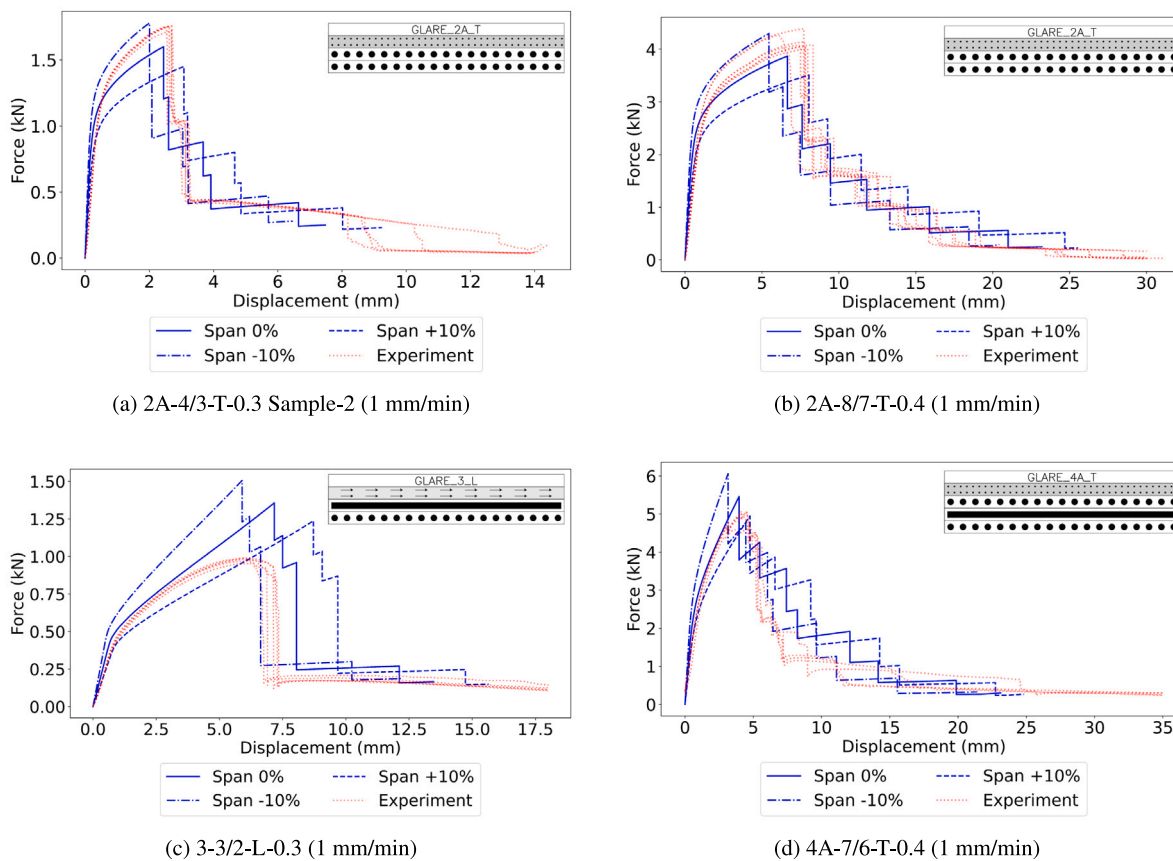

Fig. 19. Sensitivity of force versus displacement curves to span.

From the results for 4B-7/6-L-0.4 (Fig. 15), it can be seen that the number of specimens for which central cracking was observed increases with increase in displacement rate. This switch to central cracking with the increase in displacement rate is further discussed in Section 4.3.

4.3. Effect of displacement rate

Bending tests were carried out at 4 different displacement rates (1 mm/min, 10 mm/min, 100 mm/min and 1000 mm/min) to study the effect of displacement rate on failure mechanism and energy absorption of the GLARE samples. For most of the cases, the effect of displacement rate on the results is found to be minimal (Fig. 14 shows two examples), except for cases where a shift in the failure mechanism is observed. For the two examples presented in Fig. 14, the initial non-linear toe region is removed by applying a toe compensation at 2.5% of the observed peak load. It can then be observed from Fig. 14 that the effect of change in displacement rate was minimal, an increase in peak force with increase in displacement rate can be observed, however, the
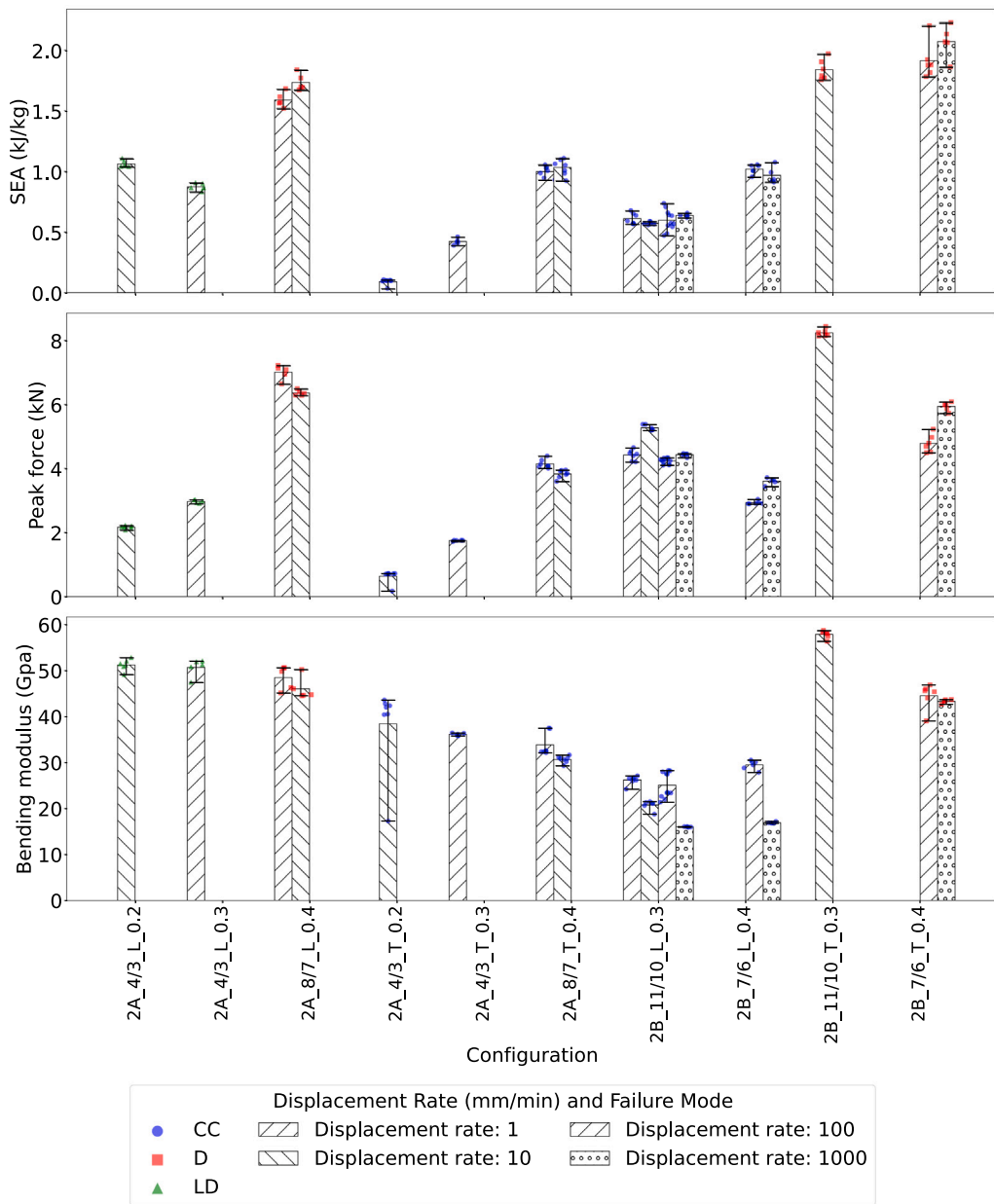
Fig. 20. Specific Energy Absorption (SEA), Peak force (kN) and bending modulus (GPa) for GLARE-2.

envelope boundaries for the peak are not well defined and there was overlap between the envelopes for different displacement rates.

For the exceptions, a switch from shear dominated failure (delamination and limited delamination) to central cracking is observed, with specimens failing in shear dominated failure recording a higher SEA compared to specimens failing with central cracking (Appendix). This switch can be explained by an increase in interlaminar fracture toughness with increasing the displacement rate [19], such that the force threshold for shear dominated failure exceeds the force threshold for central cracking failure. Fig. 15 shows a comparison of number of specimens that failed through central cracking and shear dominated failure mechanisms. A clear trend of increasing central-cracking failures with increase in displacement rates is observed.

4.4. Effect of aluminum rolling direction

To study the effect of rolling direction, a comparison can be made between the specimens 4A-7/6-L-0.4, 4A-7/6-T-0.4, 4B-7/6-L-0.4 and

4B-7/6-T-0.4. These specimens are chosen because the only difference between 4A-7/6-T-0.4 and 4B-7/6-L-0.4, and between 4A-7/6-L-0.4 and 4B-7/6-T-0.4, is the aluminum rolling direction. The comparison for both the combinations are presented below:

1. **Comparison between 4A-7/6-L-0.4 and 4B-7/6-T-0.4:**
   For both the configurations shear dominated failure is the primary failure mechanism. As observed from Fig. 16(a), while there is no significant change in bending stiffness, a slight increase in mean peak force is observed for the case with longitudinal aluminum rolling direction (4A-7/6-L-0.4: 6.38 kN and 4B-7/6-T-0.4: 5.49 kN). The average SEA is found to be similar for both configurations, 4A-7/6-L-0.4: 1.59 kJ/kg and 4B-7/6-T-0.4: 1.68 kJ/kg.

2. **Comparison between 4A-7/6-T-0.4 and 4B-7/6-L-0.4:**
   As shown in Fig. 16(b), no significant change in bending stiffness is observed, however, a slight increase in mean peak force was recorded (4A-7/6-T-0.4: 4.92 kN and 4B-7/6-L-0.4: 5.11 kN). An
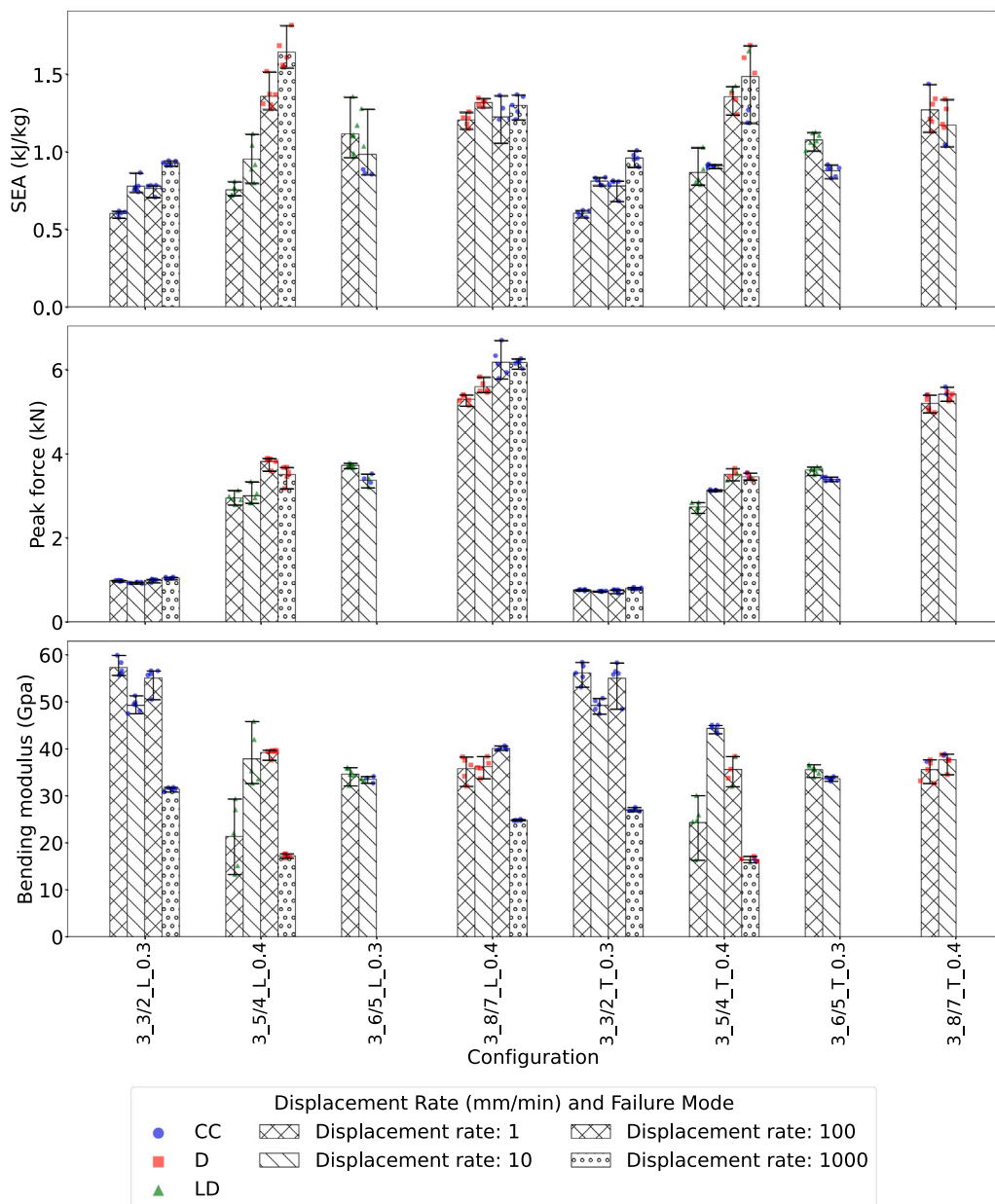
Fig. 21. Specific Energy Absorption (SEA), Peak force (kN) and bending modulus (GPa) for GLARE-3.

increase in the SEA is also observed from 1.12 kJ/kg for 4A-7/6-T-0.4 (transverse aluminum rolling direction) to 1.38 kJ/kg for 4B-7/6-L-0.4 (longitudinal aluminum rolling direction). Most of the specimens failed through central cracking (26 out of 40); however, it is important to note that configurations which showed an increase in SEA failed with shear dominated failure (delamination and limited delamination) as the major failure mode.

4.5. Results from semi-analytical model

This section is divided into two parts, the first sub-subsection compares the predictions of the semi-analytical model with experimental results for central cracking cases, the model should be more accurate for these cases as central cracking cases are driven by tensile and compressive failure of layers which are both taken into account in the model. The second sub-subsection compares the predictions of the model against experimental data for shear dominated failure cases,

while delamination and shear are not captured by the model, the model should still be able to capture the initial part of the force vs. displacement curve before a major delamination appears.

4.5.1. Semi-analytical model: Central cracking

For central cracking of 2A-T or 2B-L laminates, which have all glass fiber plies oriented in the 90° direction, the semi-analytical model predicts the slope accurately up to the failure of the first aluminum layer and is able to also capture the subsequent load drops with reasonable accuracy. For cases where the laminate includes a mix of 0° and 90° plies, the model still predicts the force-versus-displacement response well up to the failure of the first aluminum or 0° glass fiber layer. While the load drops are not predicted as precisely as in the 2A-T and 2B-L cases, the fit remains sufficiently accurate to yield reasonable energy absorption estimates—which are the primary design driver for crash structure applications. The discrepancies in load drop predictions can be attributed to the model's assumptions and limitations, particularly its inability to account for partial damage within a ply. For thin samples
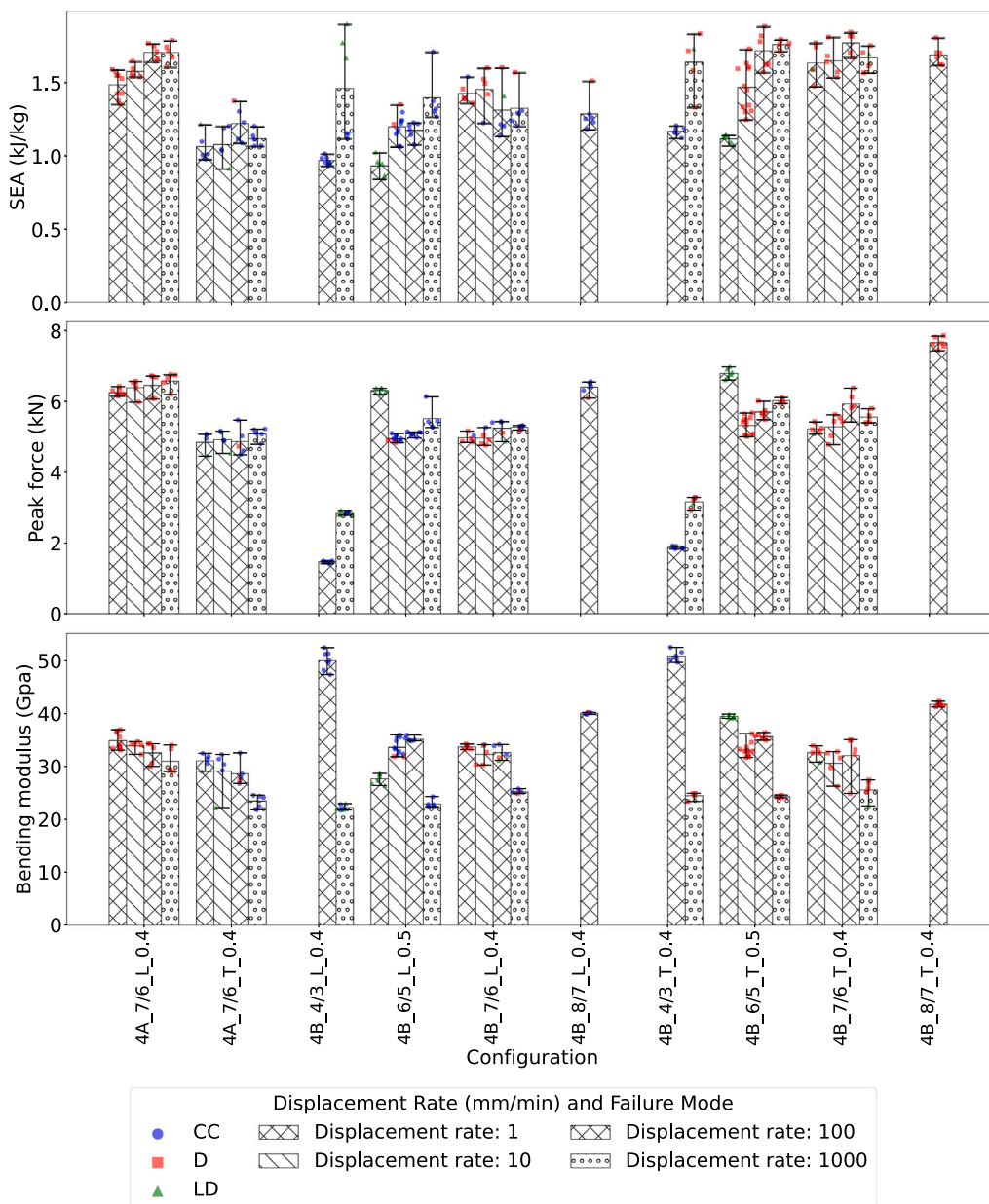
Fig. 22. Specific Energy Absorption (SEA), Peak force (kN) and bending modulus (GPa) for GLARE-4.

exhibiting central cracking failure — such as 3-3/2-L-0.3 — the semi-analytical model accurately predicts the initial stiffness (slope) up to a certain point. Beyond this point, the experimental force–displacement curve begins to smooth out and drop (see Fig. 17(b)). This behavior is likely due to slippage at the supporting pins during the test, which effectively increases the span as the experiment progresses. As a result, both the peak load and the energy absorption capacity appear reduced compared to the model predictions. An example for a laminate with all plies in 90° direction is presented in Fig. 17(a) and examples of laminates with plies in both 0° and 90° directions are presented in Figs. 17(b) to 17(d).

Peak force and SEA predicted by the semi-analytical model for central-cracking are found to be close to experimental values, coefficient of determination $R^2_{Peak-force} = 0.94$ and $R^2_{SEA} = 0.88$ (Fig. 18).

4.5.2. Semi-analytical model: Shear dominated failure

For the two shear dominated failure mechanisms herein identified, i.e. delamination and limited delamination; the proposed model still

predicts the initial slope accurately (Figs. 17(e) and 17(f)). However, as anticipated, the peak force and load drops are not accurately captured as the model does not account for shear and delamination failure. The ability of the model to predict the initial stiffness suggests its potential applicability for bending calculations in cases where damage evolution is not considered.

4.6. Sensitivity of force–displacement curve to span

During the 3-point bending tests, an error of only 2 mm in the test setup can result in a variation of about ±10% in span for some of the configurations. Additionally, during the bending process, slippage at the support pins can add to errors in the force–displacement curves. In view of the reasons highlighted above, it is important to use the semi-analytical model for studying the sensitivity of force–displacement curve to span. In this section four cases are studied, for all the four cases the span was varied by ±10% and the force-versus-displacement curves were plotted (Fig. 19). A decrease in span length (−10%) leads

Table 6

Effect of span variation on maximum force and total energy absorbed. Values in parentheses represent percentage change relative to 0% span.

Configuration	Change in span length (%)					
	0%		−10%		+10%	
	Peak force (kN)	Energy (J)	Peak force (kN)	Energy (J)	Peak force (kN)	Energy (J)
2A-4/3-T-0.3	1.60	5.74	1.78 (+11.25%)	5.36 (−6.62%)	1.45 (−9.38%)	6.43 (+12.02%)
2A-8/7-T-0.4	3.87	38.64	4.30 (+11.11%)	35.88 (−7.14%)	3.51 (−9.30%)	41.80 (+8.18%)
3-3/2-L-0.3	1.36	8.36	1.51 (+11.03%)	7.91 (−5.38%)	1.24 (−8.82%)	9.04 (+8.13%)
4A-7/6-T-0.4	5.46	43.06	6.06 (+10.99%)	38.97 (−9.50%)	4.95 (−9.34%)	45.17 (+4.90%)

Table 7

Configurations tested at displacement rate = 1 mm/min

S.No.	Configuration	No. of specimens	Average dimensions (mm)			Span	Span-analytical	STR
			Length	Width	Thickness	(mm)	(mm)	
1	2A-4/3-0.3-L	5	148.81	21.49	2.02	20.20	22.00	10.89
2	2A-4/3-0.3-T	5	151.31	21.85	2.02	20.20	20.20	10.00
3	2A-8/7-0.4-L	5	151.97	21.86	5.08	50.80	55.00	10.83
4	2A-8/7-0.4-T	7	150.97	21.32	5.08	50.80	50.80	10.00
5	2B-11/10-0.3-L	7	151.86	21.57	6.05	60.00	55.00	9.09
6	3-3/2-0.3-L	5	149.25	20.10	1.62	18.00	32.40	20.00
7	3-3/2-0.3-T	5	148.98	20.29	1.62	18.00	32.40	20.00
8	3-5/4-0.4-L	5	150.03	20.67	3.00	30.00	30.00	10.00
9	3-5/4-0.4-T	5	149.84	20.05	3.00	30.00	30.00	10.00
10	3-6/5-0.3-L	6	150.17	21.91	3.20	32.00	32.00	10.00
11	3-6/5-0.3-T	7	150.16	21.97	3.20	32.00	32.00	10.00
12	3-8/7-0.4-L	5	149.49	20.72	5.11	51.10	51.10	10.00
13	3-8/7-0.4-T	6	149.95	20.71	5.11	51.10	51.10	10.00
14	4A-7/6-0.4-L	9	151.01	20.87	5.20	52.00	52.00	10.00
15	4A-7/6-0.4-T	5	150.70	20.79	5.20	52.00	52.00	10.00
16	4B-6/5-0.5-L	6	151.48	21.26	4.99	49.90	36.00	7.21
17	4B-6/5-0.5-T	6	150.33	21.26	4.99	49.90	40.00	8.02
18	4B-7/6-0.4-L	5	149.82	20.95	5.20	52.00	52.00	10.00
19	4B-7/6-0.4-T	5	149.74	20.86	5.20	52.00	52.00	10.00

Table 8

Configurations tested at displacement rate = 10 mm/min

S.No.	Configuration	No. of specimens	Average dimensions (mm)			Span	Span-analytical	STR
			Length	Width	Thickness	(mm)	(mm)	
1	2A-4/3-0.2-L	6	149.72	21.09	1.58	18.00	20.20	12.78
2	2A-4/3-0.2-T	7	149.35	21.35	1.58	18.00	20.20	12.78
3	2A-8/7-0.4-L	5	149.59	20.87	5.08	50.80	55.00	10.83
4	2A-8/7-0.4-T	7	149.76	20.63	5.08	50.80	50.80	10.00
5	2B-11/10-0.3-L	6	151.87	21.03	6.02	60.00	45.00	7.48
6	2B-11/10-0.3-T	6	150.07	20.47	6.02	60.00	60.20	10.00
7	3-3/2-0.3-L	6	149.81	21.57	1.45	18.00	29.00	20.00
8	3-3/2-0.3-T	5	148.86	21.54	1.45	18.00	29.00	20.00
9	3-5/4-0.4-L	5	149.42	20.91	2.71	27.10	30.00	11.07
10	3-5/4-0.4-T	5	149.57	21.38	2.71	27.10	30.00	11.07
11	3-6/5-0.3-L	5	150.22	20.63	3.17	31.70	31.70	10.00
12	3-6/5-0.3-T	6	149.85	20.40	3.17	31.70	31.70	10.00
13	3-8/7-0.4-L	5	149.61	20.74	5.11	51.10	51.10	10.00
14	3-8/7-0.4-T	6	149.77	20.70	5.11	51.10	51.10	10.00
15	4A-7/6-0.4-L	5	150.70	20.79	5.20	52.00	52.00	10.00
16	4A-7/6-0.4-T	5	148.87	20.96	5.20	52.00	52.00	10.00
17	4B-6/5-0.5-L	11	149.86	21.35	5.10	51.00	51.00	10.00
18	4B-6/5-0.5-T	12	149.87	21.27	5.10	51.00	51.00	10.00
19	4B-7/6-0.4-L	5	149.88	20.95	5.20	52.00	52.00	10.00
20	4B-7/6-0.4-T	5	149.76	20.87	5.20	52.00	52.00	10.00

to an increase in peak force but a reduction in total energy absorption, whereas an increase in span length (+10%) shows the opposite trend. Notably, the relative change in peak force approximately mirrors the span variation in magnitude but with an opposite sign, indicating almost linear sensitivity of peak force to the span length (see Table 6).

5. Conclusions

Following conclusions can be made from the discussions:

1. Dependence on stacking sequence:

(a) GLARE 2 has either all plies in 0° or in 90°. Specimens with all glass fiber plies in 0° show shear dominated failure (delamination and limited delamination) for all specimens; and specimens with all glass fiber plies in 90° show central cracking failure. Configurations with all glass fibers in 0° direction show a much higher average SEA as compared to configurations with all glass fibers in 90° direction.

(b) GLARE 3 specimens, consisting of an equal ratio of 0° and 90° plies, exhibited two distinct failure modes. Approximately half of the specimens failed through shear

Table 9

Configurations tested at displacement rate = 100 mm/min

S.No.	Configuration	No. of specimens	Average dimensions (mm)			Span	Span-analytical	STR
			Length	Width	Thickness	(mm)	(mm)	
1	2B-7/6-0.4-L	6	149.55	20.99	4.49	44.90	50.00	11.14
2	2B-7/6-0.4-T	6	147.62	21.24	4.49	44.90	55.00	12.25
3	2B-11/10-0.3-L	11	149.82	20.95	5.98	59.80	55.00	9.20
4	3-3/2-0.3-L	5	150.00	21.10	1.45	18.00	29.00	20.00
5	3-3/2-0.3-T	5	149.23	21.09	1.45	18.00	29.00	20.00
6	3-5/4-0.4-L	6	149.80	21.08	3.10	31.00	31.00	10.00
7	3-5/4-0.4-T	5	150.00	21.06	3.10	31.00	31.00	10.00
8	3-8/7-0.4-L	5	149.94	21.12	5.28	52.80	52.80	10.00
9	4A-7/6-0.4-L	5	150.51	20.82	5.20	52.00	52.00	10.00
10	4A-7/6-0.4-T	5	149.39	20.97	5.20	52.00	52.00	10.00
11	4B-4/3-0.4-L	7	149.54	21.41	3.01	30.10	60.20	20.00
12	4B-4/3-0.4-T	6	149.50	21.35	3.01	30.10	60.20	20.00
13	4B-6/5-0.5-L	6	149.67	21.14	4.98	49.80	49.80	10.00
14	4B-6/5-0.5-T	6	149.67	21.36	4.98	49.80	49.80	10.00
15	4B-7/6-0.4-L	5	149.86	20.96	5.20	52.00	52.00	10.00
16	4B-7/6-0.4-T	5	149.74	20.80	5.20	52.00	52.00	10.00
17	4B-8/7-0.4-L	6	149.76	21.22	5.82	58.20	58.20	10.00
18	4B-8/7-0.4-T	6	149.87	21.17	5.82	58.20	58.20	10.00

Table 10

Configurations tested at displacement rate = 1000 mm/min

S.No.	Configuration	No. of specimens	Average dimensions (mm)			Span	Span-analytical	STR
			Length	Width	Thickness	(mm)	(mm)	
1	2B-7/6-0.4-L	5	149.48	21.01	4.49	44.90	44.90	10.00
2	2B-7/6-0.4-T	5	147.80	21.09	4.49	44.90	55.00	12.25
3	2B-11/10-0.3-L	5	149.77	21.34	5.98	59.80	55.00	9.20
4	3-3/2-0.3-L	5	148.59	21.05	1.45	18.00	29.00	20.00
5	3-3/2-0.3-T	5	149.20	21.02	1.45	18.00	29.00	20.00
6	3-5/4-0.4-L	5	149.64	21.01	3.10	31.00	31.00	10.00
7	3-5/4-0.4-T	6	149.33	21.03	3.10	31.00	31.00	10.00
8	3-8/7-0.4-L	5	149.86	21.20	5.28	52.80	52.80	10.00
9	4A-7/6-0.4-L	5	150.70	20.84	5.20	52.00	52.00	10.00
10	4A-7/6-0.4-T	5	149.50	21.10	5.20	52.00	52.00	10.00
11	4B-4/3-0.4-L	6	149.76	21.39	3.01	30.10	36.00	11.96
12	4B-4/3-0.4-T	5	149.57	21.29	3.01	30.10	36.00	11.96
13	4B-6/5-0.5-L	5	149.60	21.28	4.98	49.80	49.80	10.00
14	4B-6/5-0.5-T	4	149.58	21.21	4.98	49.80	49.80	10.00
15	4B-7/6-0.4-L	5	149.86	20.91	5.20	52.00	52.00	10.00
16	4B-7/6-0.4-T	5	149.78	20.83	5.20	52.00	52.00	10.00

dominated failure mechanisms, while the other half failed due to central cracking.

(c) GLARE 4A and 4B specimens with a 2:1 ratio between fibers in 0° (longitudinal) and 90° (transverse) direction exhibit shear dominated failure mechanism. Central cracking was however observed for one case which was tested at b/h ratio of 20 instead of 10. This indicates that an increase in b/h ratio can result in a switch from shear dominated failure to central cracking due to a decrease in shear forces.

(d) GLARE 4A and 4B specimens with a 2:1 ratio between fibers in 90° (transverse) and 0° (longitudinal) direction exhibit a combination of central cracking and shear dominated failure mechanisms.

2. Most of the cases were found to be displacement rate insensitive for the tested displacement rates (1,10,100 and 1000 mm/min), recording minimal changes as a result of change in displacement rate. However, for some configurations a shift from shear dominated failure to central cracking was observed with increase in displacement rate which can be explained by an increase in

interlaminar fracture toughness with an increase in displacement rate, resulting in the threshold for shear dominated failure exceeding the threshold for central cracking failure.

3. For specimens with longitudinal aluminum rolling direction, a slight increase in peak force was observed as compared to specimens with transverse rolling direction. For cases where majority of the fibers had a 90° orientation (4A-7/6-T-0.4 and 4B-7/6-L-0.4), a shift from central cracking to shear dominated failure was observed at lower displacement rates for specimens with longitudinal aluminum rolling direction. However, it is important to note that these two conclusions are based on the results from the two comparative cases that have been evaluated in this experimental campaign, additional data is therefore required to validate these findings.

4. The proposed semi-analytical model can be used to predict the Force-versus-displacement response of GLARE laminates under 3-point bending, when central cracking is the main failure mechanism. Improving the shear module should extend this model to cases with shear dominated failure, enabling accurate predictions of the peak load.

Table 11

Force versus displacement curves: Experiment versus semi-analytical model.
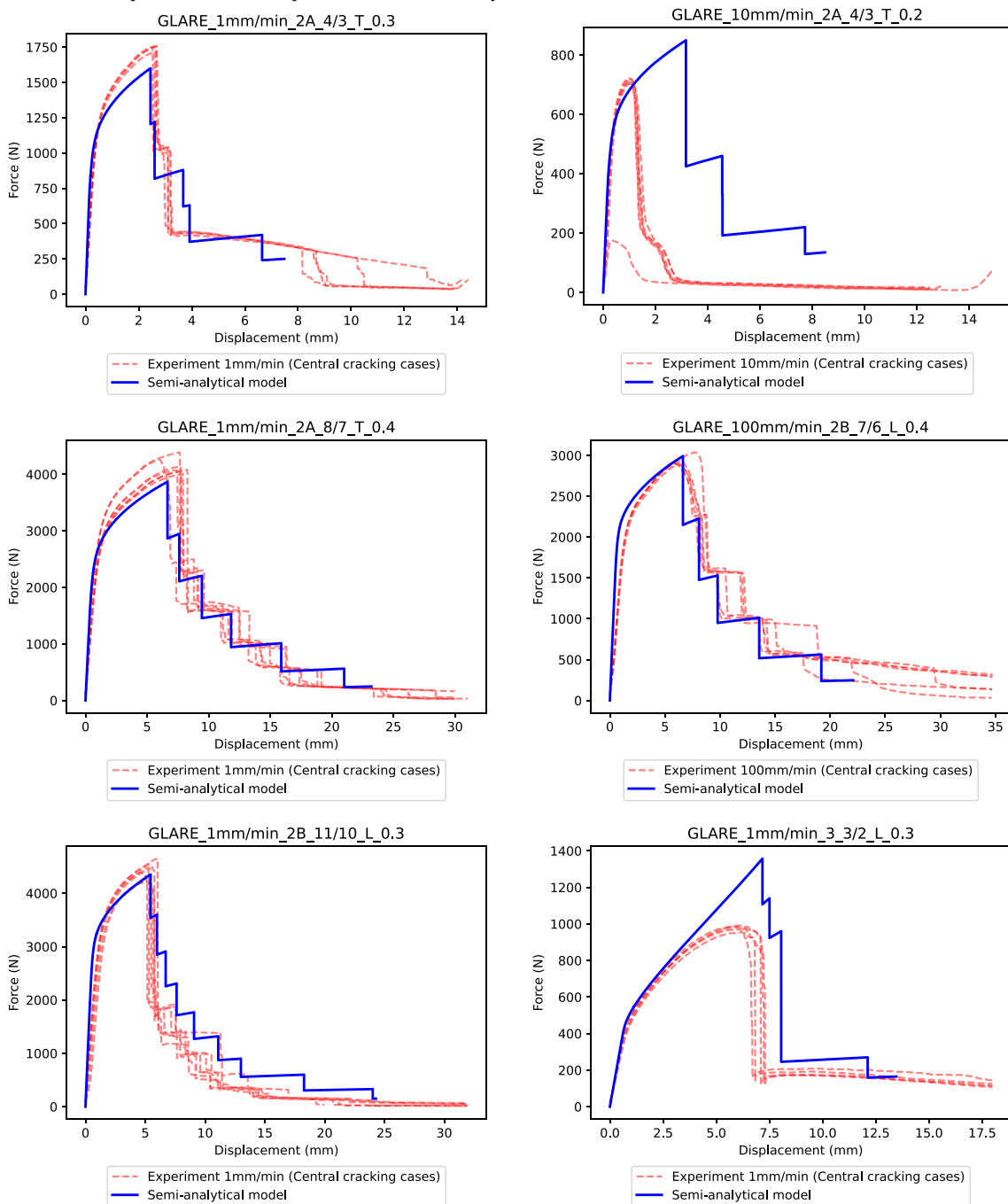
(continued on next page)

CRediT authorship contribution statement

Shreyas Anand: Writing – original draft, Visualization, Validation, Software, Methodology, Formal analysis, Data curation. **Nachiket Dighe:** Writing – original draft, Methodology, Investigation, Data curation. **Pranshul Gupta:** Methodology, Investigation, Data curation. **René Alderliesten:** Writing – review & editing, Supervision, Resources, Project administration, Funding acquisition, Conceptualization. **Saullo G.P. Castro:** Writing – review & editing, Supervision, Resources, Methodology, Conceptualization.

Declaration of competing interest

The authors declare that they have no known competing financial interests or personal relationships that could have appeared to influence the work reported in this paper.

Acknowledgments

Table 11 (*continued*).

GLARE_1mm/min_3_3/2_T_0.3

GLARE_10mm/min_3_5/4_T_0.4

GLARE_10mm/min_3_6/5_L_0.3

GLARE_10mm/min_3_6/5_T_0.3


GLARE_100mm/min_3_8/7_L_0.4

GLARE_10mm/min_3_8/7_T_0.4

Appendix

Datasets for the tested configurations at different displacement rates along with their dimensions are presented in Appendcies A.1 to A.4. STR in tables below stands for Span-to-Thickness Ratio.

Span values listed under "Span (mm)" in the tables correspond to span values calculated per Eq. (1) whereas "Span-analytical (mm)" refers to values used for the semi-analytical model. Discrepancy between "Span (mm)" and "Span-analytical (mm)" can be observed for some of the tested configurations listed below. The discrepancy in these two quantities can be attributed to errors made during experimentation or data reporting, which lead to significant errors in the initial slope predicted by the semi-analytical model when compared against experimental data-suggesting an error in reported span. Notable examples include the cases 1 mm/min-3-3/2-0.3-L and 1 mm/min-3-3/2-0.3-T, where the analytical model indicates a Span-to-Thickness Ratio (STR) of 20 instead of 10 given by Eq. (1). For consistency, span-analytical values have been used for calculation of bending strength, energy absorption and bending modulus in Appendix A.5. However, due to the absence of test video recordings, these span values approximated using the proposed semi-analytical model could not be independently verified, and should therefore be interpreted with caution.

Table 11 (*continued*).

GLARE_1mm/min_4A_7/6_T_0.4

GLARE_100mm/min_4B_4/3_L_0.4

GLARE_100mm/min_4B_4/3_T_0.4

GLARE_10mm/min_4B_6/5_L_0.5

GLARE_10mm/min_4B_7/6_L_0.4

GLARE_100mm/min_4B_8/7_L_0.4
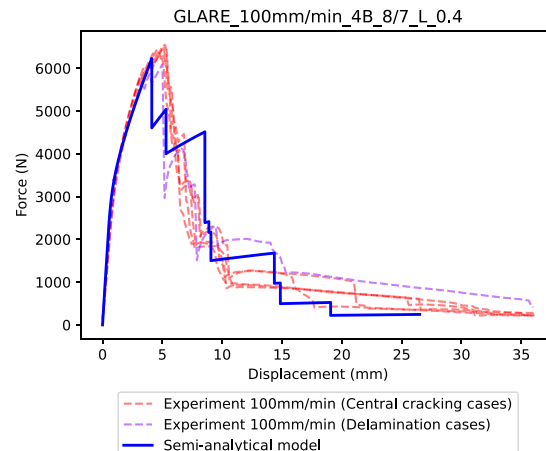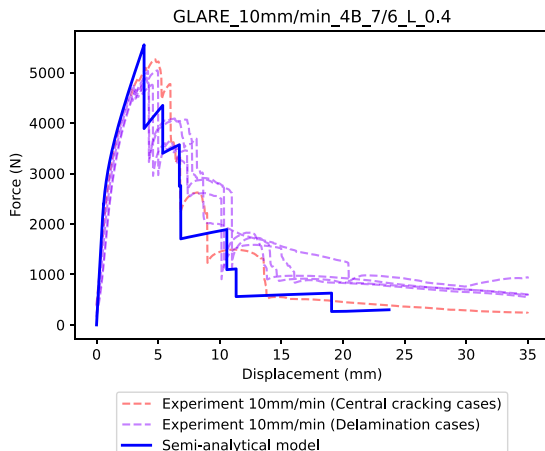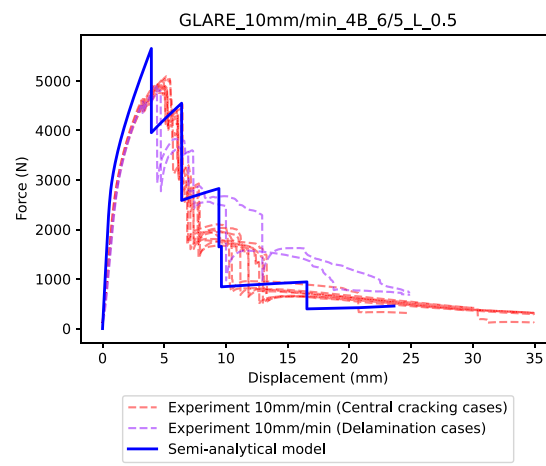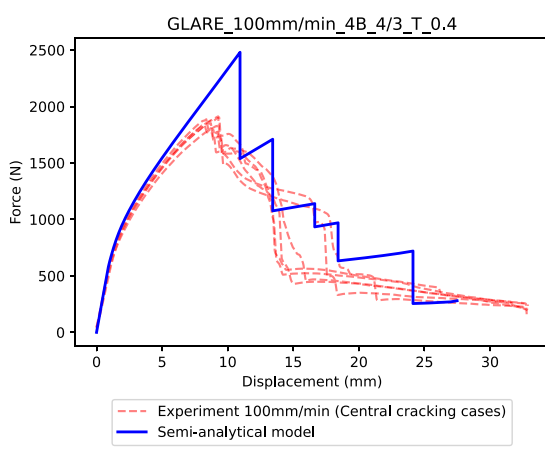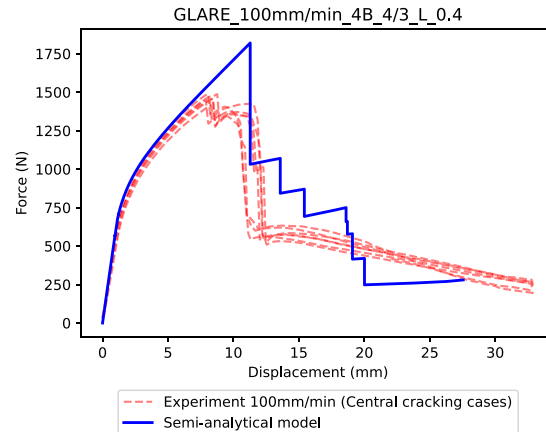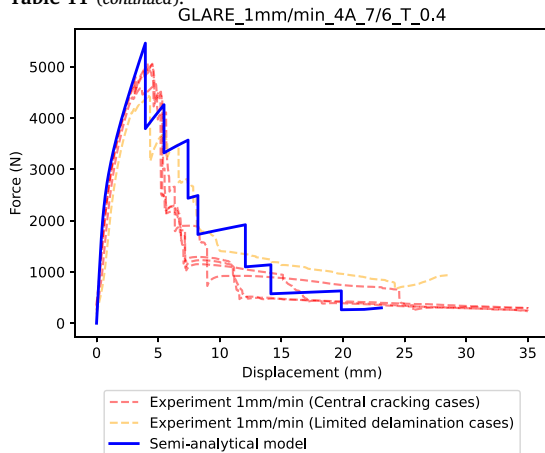
A.1. Configurations tested at displacement rate = 1 mm/min

See Table 7.

A.2. Configurations tested at displacement rate = 10 mm/min

See Table 8.

A.3. Configurations tested at displacement rate = 100 mm/min

See Table 9.

A.4. Configurations tested at displacement rate = 1000 mm/min

See Table 10.

A.5. Specific Energy Absorption (SEA), peak force (kN) and bending modulus (GPa) for experimental 3-point bending

See Figs. 20–22.

A.6. Comparison of results from semi-analytical model to experimental results

See Table 11.

Data availability

Concise data used for the paper has been provided in the appendix. A detailed dataset including all the implemented algorithms is publicly available [18].

References

[1] C.D. Rans, 2 - bolted joints in glass reinforced aluminium (glare) and other hybrid fibre metal laminates (FML), in: Pedro Camanho, Liyong Tong (Eds.), Composite Joints and Connections, in: Woodhead Publishing Series in Composites Science and Engineering, Woodhead Publishing, ISBN: 978-1-84569-990-1, 2011, pp. 35–76, http://dx.doi.org/10.1533/9780857094926.1.35, URL https://www.sciencedirect.com/science/article/pii/B9781845699901500028.

[2] Matthijs Plokker, Derk Daverschot, Thomas Beumler, Hybrid structure solution for the A400m wing attachment frames, in: M.J. Bos (Ed.), ICAF 2009, Bridging the Gap Between Theory and Operational Practice, Springer Netherlands, Dordrecht, ISBN: 978-90-481-2746-7, 2009, pp. 375–385.

[3] Ad Vlot, Glare in Europe — a long, long runway (1988–1997), in: Glare: History of the Development of a New Aircraft Material, Springer Netherlands, Dordrecht, ISBN: 978-0-306-48398-1, 2001, pp. 111–139, http://dx.doi.org/10.1007/0-306-48398-X_4.

[4] Wilco Oosterom, Roelof Vos, Conceptual design of a flying-v aircraft family, in: AIAA AVIATION 2022 Forum, American Institute of Aeronautics and Astronautics, 2022, http://dx.doi.org/10.2514/6.2022-3200.

[5] Cheng Liu, Dandan Du, Huaguan Li, Yubing Hu, Yiwei Xu, Jingming Tian, Gang Tao, Jie Tao, Interlaminar failure behavior of GLARE laminates under short-beam three-point-bending load, Compos. Part B: Eng. (ISSN: 1359-8368) 97 (2016) 361–367, http://dx.doi.org/10.1016/j.compositesb.2016.05.003, URL https://www.sciencedirect.com/science/article/pii/S135983681630573X.

[6] Huaguan Li, Yiwei Xu, Xiaoge Hua, Cheng Liu, Jie Tao, Bending failure mechanism and flexural properties of GLARE laminates with different stacking sequences, Compos. Struct. (ISSN: 0263-8223) 187 (2018) 354–363, http://dx.doi.org/10.1016/j.compstruct.2017.12.068, URL https://www.sciencedirect.com/science/article/pii/S0263822317319566.

[7] M. Harish Kumar, N. Rajesh Mathivanan, Satish Kumar, Experiment investigations of effect of laminate thickness on flexural properties of GLARE and GFRP laminates, Mater. Res. Express (ISSN: 20531591) 6 (2019) http://dx.doi.org/10.1088/2053-1591/aaf066.

[8] Y. Solyaev, S. Lurie, O. Prokudin, V. Antipov, L. Rabinskiy, N. Serebrennikova, V. Dobryanskiy, Elasto-plastic behavior and failure of thick GLARE laminates under bending loading, Compos. Part B (ISSN: 1359-8368) 200 (2020) 108302, http://dx.doi.org/10.1016/j.compositesb.2020.108302, URL https://www.sciencedirect.com/science/article/pii/S1359836820333527.

[9] AIRBUS A350 aircraft characteristics airport and maintenance planning AC, 2021, URL https://www.airbus.com/sites/g/files/jlcbta136/files/2021-11/Airbus-Commercial-Aircraft-AC-A350-900-1000.pdf.

[10] A. Vlot, J. Gunnink, Fibre Metal Laminates: An Introduction, Springer Netherlands, ISBN: 9789401009959, 2001, http://dx.doi.org/10.1007/978-94-010-0995-9.

[11] M. Hagenbeek, Characterisation of Fibre Metal Laminates under Thermomechanical Loadings (Ph.D. thesis), Delft University of Technology, 2005.

[12] Standard test methods for flexural properties of unreinforced and reinforced plastics and electrical insulating materials, 2017, http://dx.doi.org/10.1520/D0790-17.

[13] Standard test method for flexural properties of polymer matrix composite materials, (ASTM D7264/D7264M-21) 2021, http://dx.doi.org/10.1520/D7264_D7264M-21.

[14] Zwick Roell Group, Proline Technical Datasheet, 2014, URL.

[15] Huaguan Li, Jingming Tian, Weijie Fei, Zhengdong Han, Gang Tao, Yingmei Xu, Xiaocun Xu, Jie Tao, Spring-back and failure characteristics of roll bending of glare laminates, Mater. Res. Express (ISSN: 2053-1591) 6 (2019) 0865b2, http://dx.doi.org/10.1088/2053-1591/ab2109, URL https://iopscience.iop.org/article/10.1088/2053-1591/ab2109.

[16] Yury Solyaev, Arseniy Babaytsev, Direct observation of plastic shear strain concentration in the thick GLARE laminates under bending loading, Compos. Part B: Eng. (ISSN: 1359-8368) 224 (2021) 109145, http://dx.doi.org/10.1016/J.COMPOSITESB.2021.109145.

[17] Shreyas Anand, René Alderliesten, Saullo G. Castro, Low-fidelity crashworthiness assessment of unconventional aircraft: Modelling of plastic bending, in: AIAA SCITECH 2024 Forum, American Institute of Aeronautics and Astronautics, 2024, http://dx.doi.org/10.2514/6.2024-0833.

[18] Shreyas Anand, Nachiket Dighe, Pranshul Gupta, René Alderliesten, Saullo Giovani Pereira Castro, Dataset for Glass Reinforced aluminum (GLARE) Laminates subjected to three-Point Bending, 2025, http://dx.doi.org/10.6084/m9.figshare.29590073.v1, URL https://figshare.com/articles/dataset/Dataset_for_Glass_Reinforced_aluminum_GLARE_Laminates_subjected_to_three-Point_Bending/29590073.

[19] Xiaoge Hua, Huaguan Li, Yi Lu, Yujie Chen, Liangsheng Qiu, Jie Tao, Interlaminar fracture toughness of GLARE laminates based on asymmetric double cantilever beam (ADCB), Compos. Part B: Eng. (ISSN: 1359-8368) 163 (2019) 175–184, http://dx.doi.org/10.1016/j.compositesb.2018.11.040, URL https://www.sciencedirect.com/science/article/pii/S1359836818328245.